Development and Control of Micro-Ionic Thrusters for Centimeter-Scale Aerial Robots

Hari Krishna Hari Prasad

A thesis
submitted in partial fulfillment of the
requirements for the degree of

Master of Science

University of Washington

2020

Committee:

Sawyer B. Fuller

Santosh Devasia

Igor Novosselov

Program Authorized to Offer Degree:
Mechanical Engineering

University of Washington

Abstract

Development and Control of Micro-Ionic Thrusters
for Centimeter-Scale Aerial Robots

Hari Krishna Hari Prasad

Chair of the Supervisory Committee:

As we go smaller and smaller, we take inspiration from Biology to design our Engineered machines. Currently, most centimeter-scale aerial robots use complicated, failure-prone insect-inspired flapping-wing mechanisms to propel themselves. In Electrohydrodynamics (EHD), corona discharge generates a flow of ions in an electric field between two electrodes; the high-velocity ions transfer their kinetic energy to neutral air molecules through collisions, accelerating the gas and thus creating thrust. This mechanism produces thrust without the need for any moving parts, scales favorably with diminishing size, and is a sparsely explored propulsion mechanism. In this work, laser-based microfabrication of EHD-thruster is explored. Following this, high-voltage Pulse-Width-Modulation (PWM) (achieved using a high-voltage power MOSFET) is established as a means of modulating thrust with sufficient bandwidth to perform closed-loop control.

TABLE OF CONTENTS

LIST OF FIGURES

LIST OF TABLES

GLOSSARY

ELECTROHYDRODYNAMICS (EHD): is the study of the dynamics of electrically charged fluids.

CORONA DISCHARGE: is an electric discharge brought on by the ionization of fluid surrounding an electrically charged conductor.

COULOMB FORCE: is the volumetric force acting on the positively charged species between the electrodes, which in-turn defines the theoretical maximum thrust achievable.

THRUSTER: is a device which generates a propulsive force.

EMITTER: is a high-voltage electrode which has highly localized points of electric field density to initiate corona discharge over a certain critical voltage.

COLLECTOR: is a grid-like grounded electrode which acts as a sink and absorbs positively charged species, and accommodates ensuing fluid flow.

JIG: a unit which is used to impart specific predefined structures to the final device and hold together fabricated components for ease of assembly.

PULSE-WIDTH-MODULATION (PWM): is a method of reducing the average power delivered to a load by turning a switch on and off very quickly.

SWITCHING CIRCUIT: is a high-voltage power-MOSFET based circuit used to modulate the potential of the Collector electrode with respect to the common ground through PWM.

STEP RESPONSE: is the temporal response of a system to a shift in the level of the input.

FREQUENCY RESPONSE: of a system is the combination of output magnitude and delay in responding to a spectrum of input frequency content.

CONTROL LAW: is an algorithm which determines the input to a system based on certain measured quantities.

ACKNOWLEDGMENTS

I start by expressing my unbounded gratitude, respect, and awe for my advisor, Prof. Fuller, who has been instrumental in my learning outcomes from day one of the Master's program. His unrelenting support and shower of wisdom during dark days has always sparked hope in me and is responsible for the aspiring roboticist I am today.

Next, I would like to thank Yogesh Chukewad and Johannes James for showing patience and compassion when training me. I have fond memories of our brainstorming sessions and your help has been the cornerstone for all my accomplishments during this program.

I would also like to thank all of my lab-mates for all of their inputs and encouragement during times of failure and triumph.

I thank Ravi and Prof. Novosselov for sharing their abundant knowledge and for playing a key role in our brief collaboration. My sincere thanks to Prof. Devasia for guiding me whenever I needed help, for serving on my committee, and for all his inputs in every single one of our interactions. A special thanks to Prof. Steve Brunton and Prof. Sam Burden for elegantly easing me into the vast field of Control theory, which I wouldn't want to learn in any other way.

I also thank my friends who have been a constant source of positivity and support. Finally, a special thanks to my mom, dad, brother, and all family members for constantly supporting me, for influencing my scientific temperament and reminding me that I'll always have a home to return to.

DEDICATION

to my dear mom, Revathi

Chapter 1
INTRODUCTION

1.1 Motivation

Insect-scale robotics has been an area of interest for its possible uses in agriculture, search and rescue, and biomedicine, among other areas. The small size and reduced manufacturing cost of insect robots have facilitated micro-robotic research. To date, the primary emphasis in insect-scale robotics has been on drawing inspiration from biology, because biology has found solutions whose existence proves they work. One example is flapping-wing robotic insects[32]. Robots of this type have subsequently incorporated onboard sensors for flight stabilization [17] and lifted off for the first time without needing a wire tether reaching to the ground using a laser power source [26], and subsequently, incandescent light [25]. Other developments include using explosives to break the surface tension of water [3] and RoboFly, which is capable of performing multi-modal locomotion including walking [7], flying, and air-water interfacial locomotion [6]. While flapping-wings are well suited to insect-sized aerial vehicles, they impose a significant cost in terms of mechanical complexity [46]. In this paper, we focus on an alternative means of generating thrust that is not seen in biology: electrohydrodynamic (EHD) thrust. EHD thrust requires sustained high voltage, which may be why it is not observed in biology. From an engineering perspective, EHD has the appealing characteristic that it requires no moving mechanical parts, simplifying fabrication.

1.2 Background

A recent advance indicating the promise of EHD thrust was fully EHD-powered 2.5 kg airplane [47]. The work in [11] reported the demonstration of a very small EHD-based

aircraft, the “Ionocraft” measuring only 3 cm across and consisting of four-thrusters. It was able to take off using an external power source and could carry an onboard IMU that sends data through external tethers. The strength of that work was how the low outflow velocity from low-voltage EHD thrusters was a good match to the low mass of that device. Additionally, EHD is potentially simpler than flapping-wing flight because even a four-thruster device consists of only a single moving part. However, the device in [11] was fabricated using expensive semiconductor-based cleanroom fabrication facilities. Significant engineering development is required before a small EHD-powered robot can perform aerial locomotion fully autonomously, rendering it capable of useful application. More rapid and less expensive methods to build robots with EHD propulsion could facilitate faster design iteration times, which is highly desired when technology is still in its infancy.

1.3 Main Contributions

In this work, a less precise, but much faster way of manufacturing EHD thrusters is discussed. It takes about 15 minutes to go from laser micromachined components to a complete quad-thruster array. To move towards controlled flight experiments, we need to establish at the minimum a ¿ 1 thrust-to-weight ratio and an open-loop takeoff experiment to exhibit sufficient thrusting capabilities. Earlier iterations of the quad-thruster array had the following problems:

- There was high variability in the thrust generated by the individual thrusters of the quad-thruster array. This resulted in the consistent tumbling of the robot during open-loop takeoff experiments.

- The device also displayed a peak thrust of 343.35 µm which amounts to a thrust-to-weight ratio of 0.95.

Hence, analyzing the existing assembly process and visiting the theory that governs the thrust generation in EHD powered aircraft is key to moving towards controlled flight. In

this thesis, chapter 2 discusses the following changes that were crucial in achieving open-loop liftoff for the quad-thruster array:

- Variability was an offspring of the misalignment introduced by the jig manufacturing process. This process was fixed to achieve well-aligned jigs which in-turn resulted in lesser variability between thruster in the array.

- The one-dimensional Coulomb force model is leveraged to make minimalistic parametric changes to the thruster design to achieve greater thrust at a higher operating range.

In chapter 3, the focus will be on controlling these thrusters. Noting the similarity between multi-copters and the quad-thruster array, high-voltage PWM for modulating the thrust is explored and the resulting thrust profile is characterized. Subsequently, these results are then applied to a simple 1DOF control problem to reinforce the viability of the proposed control scheme.

Chapter 2

DEVELOPMENT OF MICRO-IONIC THRUSTERS

When delving into the mesoscale, scaling physics exacerbates the development of engineered systems through traditional solutions and methods. Motors and propellers scale unfavorably due to enhanced surface effects and reduced volumetric effects at the mesoscale [23]. Researchers have turned to biology to inspire innovative solutions to the aforementioned challenges and to design mesoscale aerial robots. But, there are other attractive ways to generate thrust at this scale such as Electrohydrodynamic force in the presence of corona discharge. This is a long-studied, yet poorly understood phenomenon until very recently for mesoscale robotic propulsion - where a sharp electrode at very high potential is perpendicularly pointed towards a grid-like grounded electrode [13][11][12]. Our thruster design is inspired based on this work but uses 355 nm Diode-Pumped-Solid-State (DPSS) laser to micro-fabricate the necessary components. This doesn't require a clean-room facility and takes a couple of minutes to assemble the complete thruster array. Given the indisputable rapid-prototyping advantages, the manufactured array has its drawbacks. This chapter tackles some these problems and is organized as follows:

- a futuristic-version of the micro-ionic thruster
- Electrohydrodynamics (EHD)
- Motivation for multi-thruster arrays
- Limitations of the current design
- assembly improvements

- enhancing thrust generation
- experimental methods and open-loop liftoff
- performance comparisons
- chapter summary

2.1 A futuristic-version of the micro-ionic thruster

With the ever-increasing population, the amount of cultivable land is decreasing at an alarming pace and productivity needs to be improved to feed billions across the world. One proposed solution is smart agriculture, where each planted crop is monitored for its necessities [38] and resources are spent accordingly. This will optimize resource consumption (pesticides, fertilizers, water, etc) and increase the overall yield.
There are several similar applications that require environmental monitoring - dryness/heat content monitoring in forests prone to wildfires, disaster-prone regions, extraterrestrial exploration, etc. There is one common theme in all of these applications - **the need for high-resolution information gathering**. The ability to disperse a large-suite of sensors to monitor the environment sounds incredibly attractive. They can monitor and search for specific triggers for certain environmental events, inform favorable decisions, and improve productivity in applications like smart agriculture. Such sensors might not be needed perennially or for long-duration which is subjective to the application.
Hence, given our requirements for less-precise, high-resolution data, we are interested in bulk-manufactured, cheap, *mobile sensors* which can be deployed by a larger drone or could be payload on tiny flying insects [24]. Abundant, application-rich future awaits micro-robots to help with large-scale and granular data gathering - one such platform could be the flying-ionic-sensor suite.
The mobile ionic sensor-suite has Guidance, Navigation, and Control (GNC) unit, onboard power electronics, and communication capabilities which provides the ability to navigate to

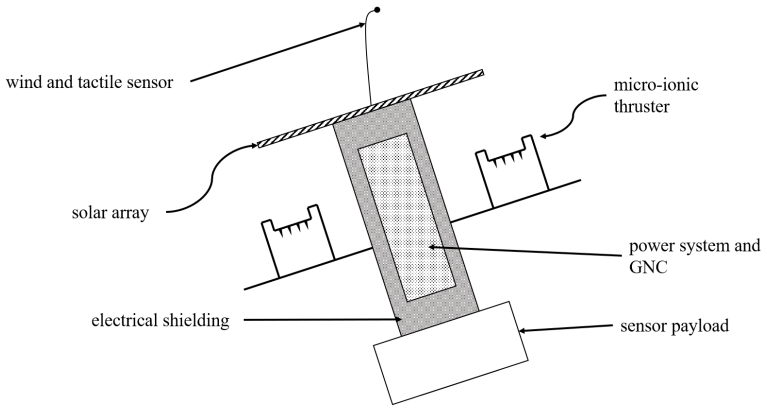

Figure 2.1: **A futuristic version of an autonomous flying sensor-suite powered by an EHD thruster array.**

a specified location and start recording data, and then change location if needed.

2.2 Electrohydrodynamics (EHD)

Electrohydrodynamics (EHD) is an interdisciplinary field describing the interaction of fluids with an electric field. Insights into complex multi-physics interactions are essential for understanding EHD flows (1) ion generation; (2) the ion motion in the electric field; (3) the interaction between the motion of ions and the neutral molecules; and (4) the inertial and viscous forces in the complex flow.

2.2.1 Corona discharge driven flow

Corona discharge generates a flow of ions in a strong electric field between two electrodes; the high-velocity ions transfer their kinetic energy to the neutral air molecules by collisions that accelerate the gas in the direction of ion drift. This electrohydrodynamic (EHD) flow propulsion phenomenon, also referred to in the literature as ionic wind, is used in many practical applications, such as convective cooling [19, 27], electrostatic precipitators (ESP)

[44], plasma-assisted combustion [28], airflow control [36, 39], and as a turbulent boundary layer actuators [5]. The corona induced EHD flow converts electric energy into kinetic energy directly and requires no moving parts. The process of corona discharge for the EHD thruster is depicted in 2.2. When the potential difference between the electrodes exceeds a certain critical value, a bipolar plasma region is formed which is responsible for the generation of positively charged ions.

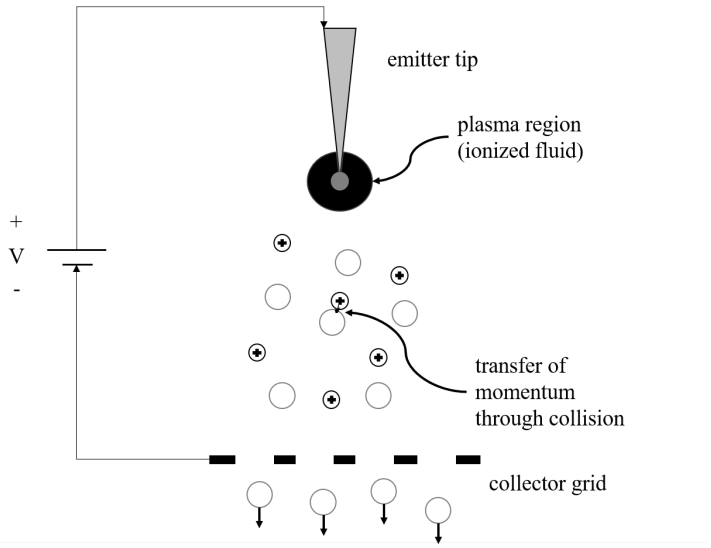

Figure 2.2: **The figures shows the transfer of momentum between the positively charged species and neutral air molecules at voltage above the critical corona onset voltage.**

The voltage-current relation during the corona discharge characterizes the ion motion between the electrodes. This phenomenon has been studied since the early 20th century. The classic relationship was derived by Townsend [42] in 1914 and validated for a coaxial corona configuration. Some recent studies modify Townsend's quadratic relationship to better describe the relationship for different electrode configurations [48, 49, 34, 20]. A generalized analytical model for voltage to current and voltage to velocity for EHD driven

flow has been recently described [20]; the analytical model has a good agreement with the experimental data in the accelerating flow regions (EHD dominated flow). The analytical study has been extended to determine the voltage-thrust relationship in planar coordinates with and without considering viscous losses and has good agreement with experiments [43] and previous work [37, 35]. Previous studies have reported that maximum velocity for point-to-ring electrode configuration was recorded at 9 m/s [21] and have assessed the use of ionic winds in propulsion applications [37].

Stuetzer [40] presented the first experimental and theoretical analysis of pressure drag produced by the ions, where he determined the pressure generation over a wide range of carrier media. Previous work performed by Masuyama [35] determined the achievable thrust to power ratios of EHD propulsion on the orders of 5-10 N.kW^{-1}. Thrust to power ratio was found to be dependent on electrode distance and the potential difference between the electrodes. Similar results were observed for an ionocraft with a wireless power supply onboard and transmitted power up to 100 W to ionocraft at the voltages up to 12 kV [29]. The EHD propulsion can be utilized for UAV propulsion; the experimentally measured maximum thrust density of 15 N.m^{-3} was reported recently [18]. Drew et al. showed that higher thrust density can be achieved for insect-scale robots [13, 11] and EHD flow can be used for flight control.

2.3 Motivation for multi-thruster arrays

Propeller-based quadcopters are attractive due to their simplicity and their control over 4-spatial DOF (3 rotational and 1 translational) which can be used to perform agile maneuvers such as multi-flips as shown in [31]. There is also evidence that as the scale of the device decreases, the maximum achievable angular acceleration increases ([30][4]) giving mesoscale MAVs their inherent instability and agility. Future versions of multi-ionic-thrusters are capable of more impressive feats given the similarity they share with propeller-based multicopters in pitch/roll dynamics and their sizes being smaller in comparison.

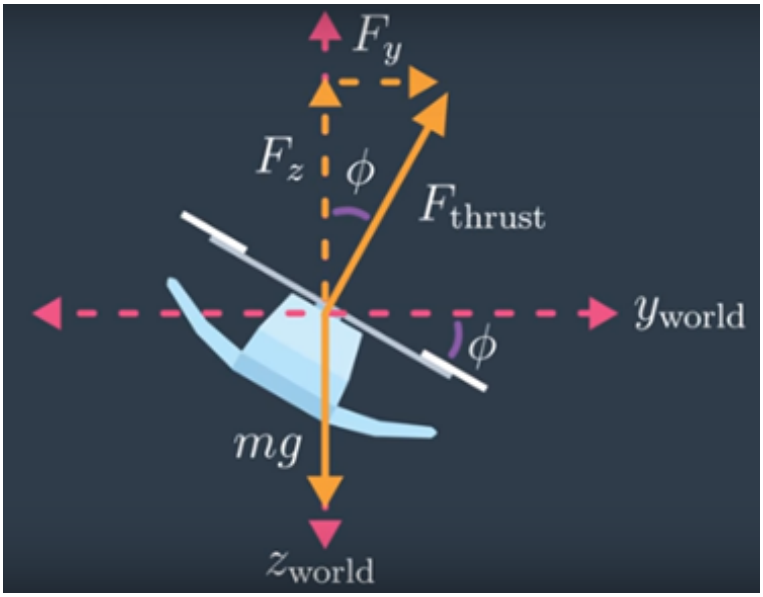

Figure 2.3: **Pitch/Roll dynamics for a multi-copter** as shown in `https://towardsdatascience.com/demystifying-drone-dynamics-ee98b1ba882f`.

Yaw control is slightly tricky due to the absence of moving parts on the device, Yaw could be achieved by tilting the thrusters inwards in a symmetric way, or the coupling between pitch and roll dynamics could be leveraged to "wriggle-steer" the heading of the device (achieve desired Yaw) [15].

2.4 Limitations of the current design

2.4.1 Thrust Measurement Method

A tweezer based holding apparatus is used to hold the thruster outside the vicinity of the precision scale. Once the device is actuated, thrust is measured as the change in the weight of the holding apparatus. Mettler Toledo ML204 precision scale is used to record the change in the weight (Fig.2.4). It has a maximum measurement range of 220 g and a resolution of 0.1 mg.

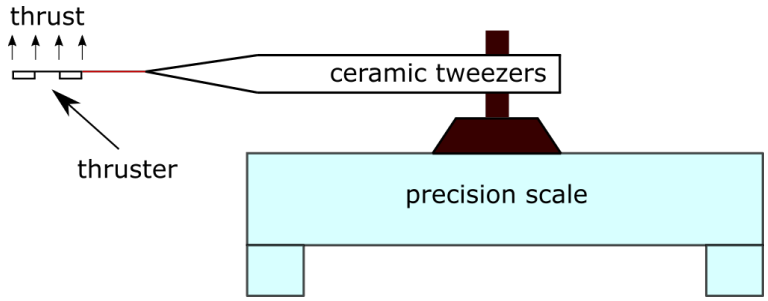

Figure 2.4: **A cartoon showing the thruster and holding apparatus shown on top of the precision scale.**

2.4.2 Thrusting Performance

The thrust measurements are taken for each thruster of the quad-thruster array. The results show high variability between the measurements for each thruster (Fig.2.5). Let us consider a specific actuation voltage 3.25 kV (**refer to the vertical line shown in Fig.2.5**), where thrusters 2 and 4 produce an average thrust of 41 µN and 43 µN, in comparison to thrusters 1 and 3 which produce 96 µN and 100 µN respectively. This amounts to a total lift force of 361 µN which is slightly above the weight of the array 343 µN. The variation in the thrust produced creates a torque of magnitude 115 µN mm, which very quickly creates a change in attitude greater than 18° where the lift generated drops below the weight of the array. Hence, this device will tumble before achieving liftoff as shown in Fig. 2.6.

Traditional methods of trimming the robot can't be applied to this problem. To correct for manufacturing-induced biases in this device using established trimming techniques for MAVs (refer [8]), thruster 1 needs to be actuated at 3.5 kV and thruster 3 at 4 kV (**refer to the horizontal line shown in Fig.2.5**) which is not feasible given the fact that high-voltage power supplies have only one output, and procuring more is inefficient. This also calls into question the quality of thruster arrays resulting from the proposed manufacturing method.

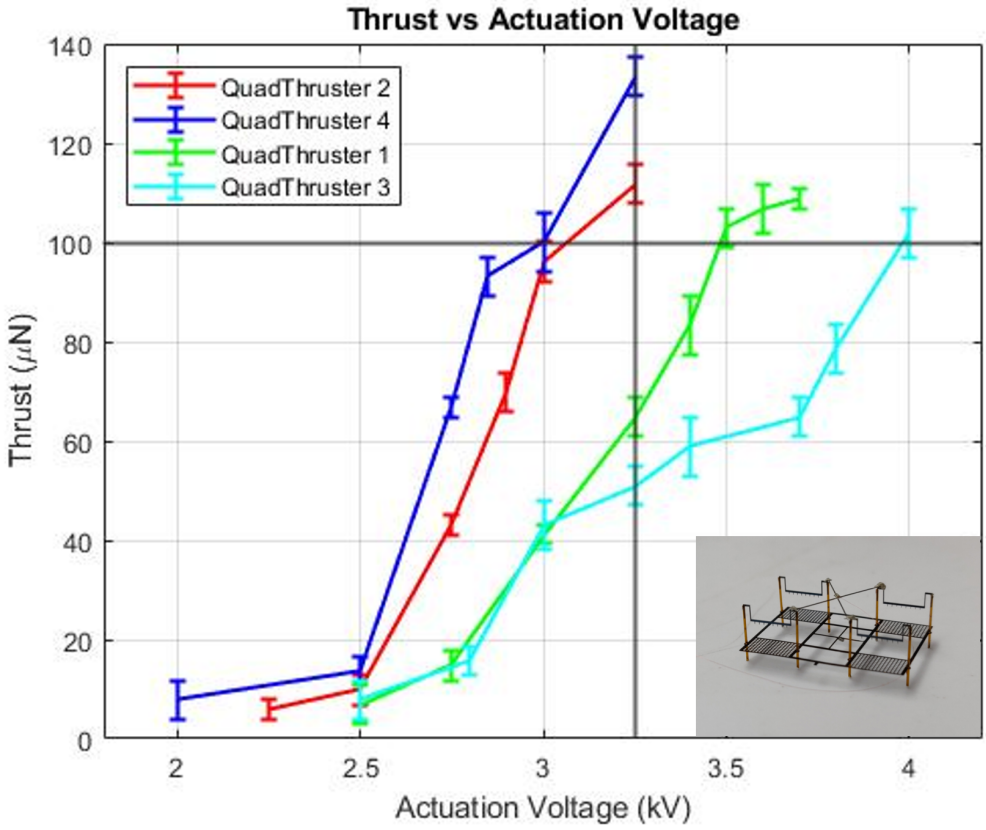

Figure 2.5: **Measured thrust values for varying voltage ranges of each thruster in the quad-thruster array.** *Inset:* A quad-thruster array

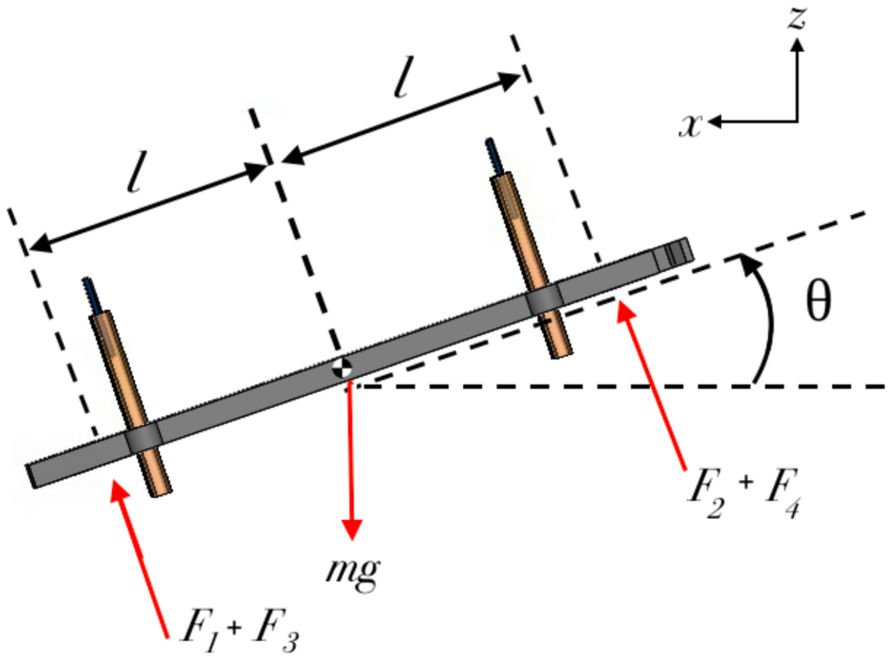

Figure 2.6: **An illustration depicting the roll/pitch dynamics of quad-thruster array and tumbling when there is significant variation in the thrust of each thruster at a given voltage.**

2.5 Assembly Improvements

2.5.1 Constituting Components

The device is made of the following components:

1. The dielectric standoffs between the ground (collector grid) and high-voltage (emitter) electrodes are made up fiber-optic glass poles of inner diameter 250 µm and outer diameter 350 µm

2. The Emitter electrode is fabricated from 100 µm-thick blue-tempered steel.

3. The Collector grid is fabricated from 80 µm-thick 0-90-0 carbon fiber composite.

2.5.2 Assembly Process

In this section, we discuss the assembly process for the quad-thruster device. The assembly takes about 15 minutes to complete after the components are fabricated. The steps involved in the assembly process are summarized below.

1. A set of eight poles is placed through holes on jig-1 as shown in Fig. 2.7 (a).

2. The grid is carefully aligned and slid through the poles; it is then glued down with these poles from top to avoid accidentally gluing the components with the jig. It then looks as shown in Fig. 2.7 (b).

3. Subsequently, four spacing jigs (having a height of 3.5 mm) are placed on each collector grid as shown in Fig. 2.7 (c).

4. Four emitters are now slid into the poles on top of each collector grid as shown in Fig. 2.7 (d). It is made sure that all of the tips are in contact with their spacing jigs. These emitters are then glued down (Cyanoacrylate) with the poles.

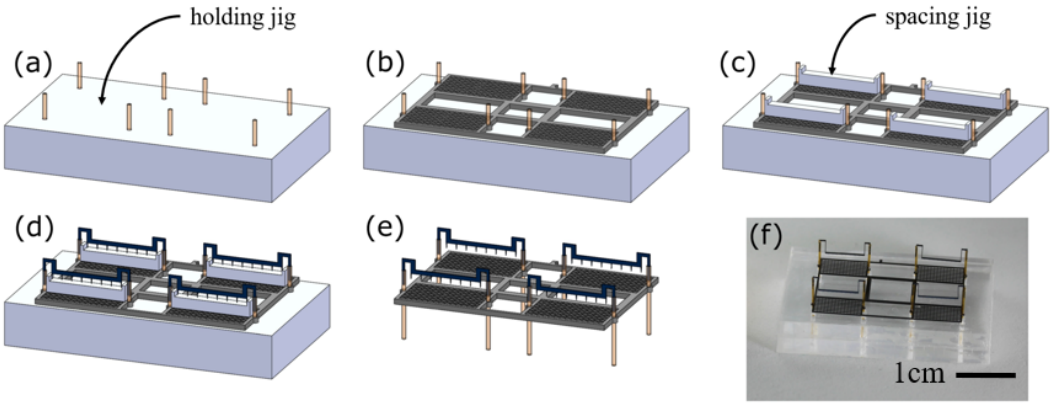

Figure 2.7: **Assembly steps of the quad-thruster device.** (a) Fiber-optic glass poles placed into the holes of the holding jig. (b) Grid is then placed on holding jig through the poles. Note: grid thickness exaggerated for 3D view. (c) Four spacing jigs placed on each single collector grid. (d) Four emitters are slid into the poles on top of spacing jigs. (e) Dimetric view of a quad-thruster after the jigs are removed. (f) Picture of a quad-thruster fully assembled in the external jig-1 that is used for assembly.

5. Once the glue is dry, all four spacing jigs are removed, and the whole assembly is then taken out of the holding jig. The assembly looks like the CAD shown in Fig. 2.7 (e). Fig. 2.7 (f) shows a picture of an actual assembly sitting on a holding jig.

6. The whole system is powered through external tethers. The quad-thruster has 2 external wires; a 58-gauge copper wire is attached to one of the inner ends of the emitters such that the connection is closer to the center of the collector grid. The other 58-gauge connection is made to the center of the collector grid. Silver paste is used to make the connections with the corresponding electrode. After an electrical connection is established, a bit of glue is added to further reinforce the joint.

2.5.3 Holding Jig

From the assembly section, it can be seen that the holding plays the most crucial role in the alignment of the thrusters of the quad-thruster array. Hence, we start by investigating its manufacturing process. These jigs are cut-out using Glowforge CO_2 laser. The intended cutting scheme is shown in Fig.2.8 b.

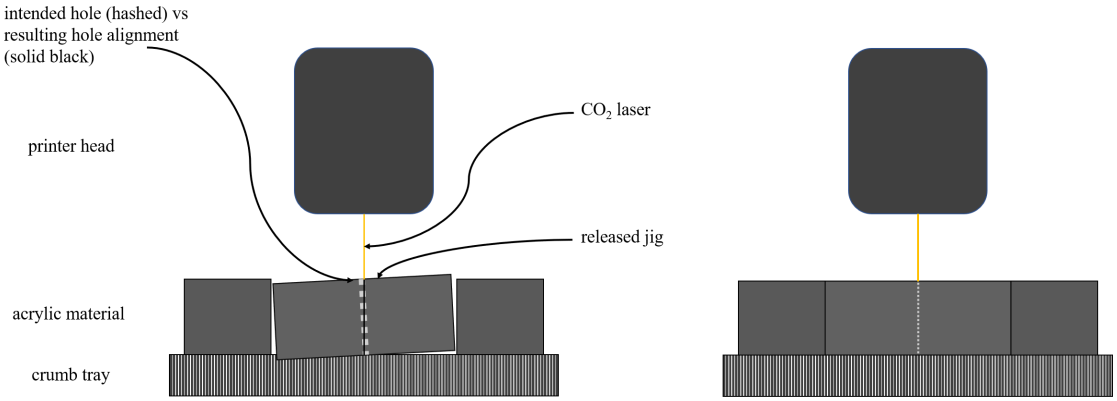

Figure 2.8: **Hole alignment during Holding jig fabrication.** (a) Release cut happening before all holes are complete results in misaligned holes. (b) Intended hole alignment

Upon closer inspection, it was revealed that the release cut for the jig was being made before all the holes were complete. This releases the jig block from the rest of the acrylic bulk rendering the surface unfocused and results in misaligned holes. Hence, the following changes were made to improve the assembly process of our device:

1. Small diagonally opposite discontinuities of width and height 100 µm were introduced into the release contour as shown in Fig.2.9. This ensures that irrespective of the cutting order, the jig blocks remain to be a part of the acrylic bulk, and thus in the focus of the laser-cutter.

2. The hole diameter is reduced from 600 µm to 400 µm(notice that there is still 50 µm cushion to accommodate for other irregularities). By sacrificing some assembling time, we achieve tighter alignment.

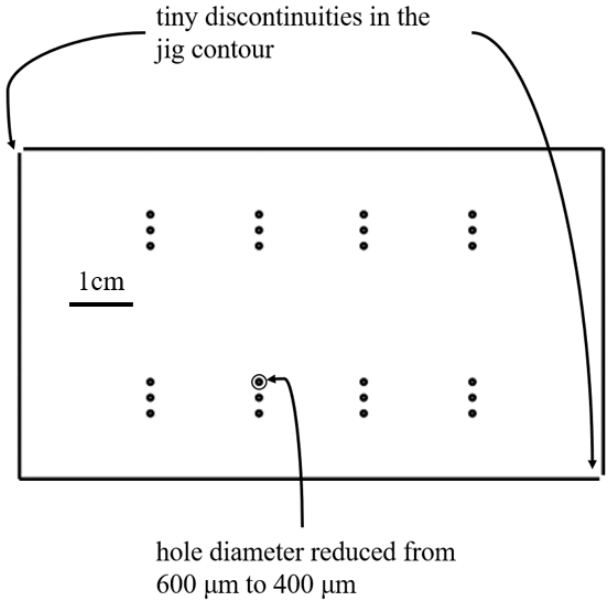

Figure 2.9: **The figure illustrates the changes made to the 2D holding jig drawing.**

2.6 Enhancing Thrust Generation

2.6.1 Electrohydrodynamic Force

A one dimensional model for an EHD thruster yields an expression in terms of the current, distance between the anode (Emitter electrode) and cathode (collector electrode). Space charge effect is ignored here, However, it can be important at high electric field strengths. The current is determined by integrating charge density,

$$I = \int J.dA = \int \rho_e E \mu dA \tag{2.1}$$

where ρ_e is the charge density, μ is the ion mobility in the air, E is the electric field. An ion mobility value of $\mu = 2 \times 10^{-4}$ m^2/V-s is assumed in this study. For energy transfer efficiency analysis, consider that thrust is equal to the Coulomb force acting on the volume of fluid between the anode and cathode,

$$F = \int \rho_e E dV = \frac{Id}{\mu} \tag{2.2}$$

where F is the thrust, I is the ion current, d is the distance between the electrodes. The corona power can be written as in Eq. 2.3 and efficiency which is defined as F/P is given by equation Eq. 2.4.

$$P = IV \tag{2.3}$$

$$\frac{F}{P} = \frac{d}{\mu V} = \frac{1}{E\mu} \tag{2.4}$$

where E is the electric field strength, and V is the applied voltage. Drew et al. report the minimum efficiency in their design should be 2 mN/W. The analysis sheds insight into the importance of the electrode distance and applied voltage. Eq. 2.4 shows that for the larger electrode spacing higher efficiency values can be reached as observed by Guan et al. [21].

Related to electrode configuration, it is important to revisit Townsend's relations [41],

$$I = CV(V - V_{crit}) \tag{2.5}$$

where V_{crit} is the onset voltage and V is the voltage applied. C is a constant related to the geometry of the electrodes [35]. Thrust can be determined using Townsend's relation

$$F = \frac{CV(V - V_{crit})d}{\mu} \tag{2.6}$$

In a practical thruster design, to achieve maximum thrust, the constant C needs to be maximized and V_{crit} needs to be minimized. Other considerations include the effects of non-linear ionization region, secondary flow structures, cathode blockage ratio, the transition from glow to streaming corona discharge, and eventually to sparkover.

2.6.2 Increasing the inter-electrode distance

Right off the bat, we notice the proportional dependence of the Coulomb force on the inter-electrode distance. For current thruster design, we are using an inter-electrode distance of 2.75 mm. And we hypothesize that **increasing the inter-electrode distance will increase the force generated at a higher operating voltage range (which compensates for the dropping current).** In simpler terms, increasing the distance will require larger voltages to drive the same amount of corona current. Hence, at a higher voltage range, we can generate more force. Thus, the inter-electrode distance was increased from 2.75 mm to 3.25 mm.

2.7 Experimental Methods and Open-loop Liftoff

2.7.1 Quantifying the Thruster Performance

The electrical characterization of each thruster in the quad thruster device was performed first. A high voltage positive DC power supply (Bertan 205B-20R) was used to create the potential difference between the emitter and the collector. The current associated with

the discharge was determined from the power supply's built-in ammeter. Four measurements are taken for the corona current and the generated thrust at each actuation voltage. The sample mean and standard deviation are computed. The error bars used in Fig. 2.10 and Fig. 2.12 denote one standard deviation from the sample mean. Results are shown in Fig. 2.10 for each of the four thrusters that comprise a single unit. The current and voltage trends are similar to previously reported quadratic trends [20, 42, 41].

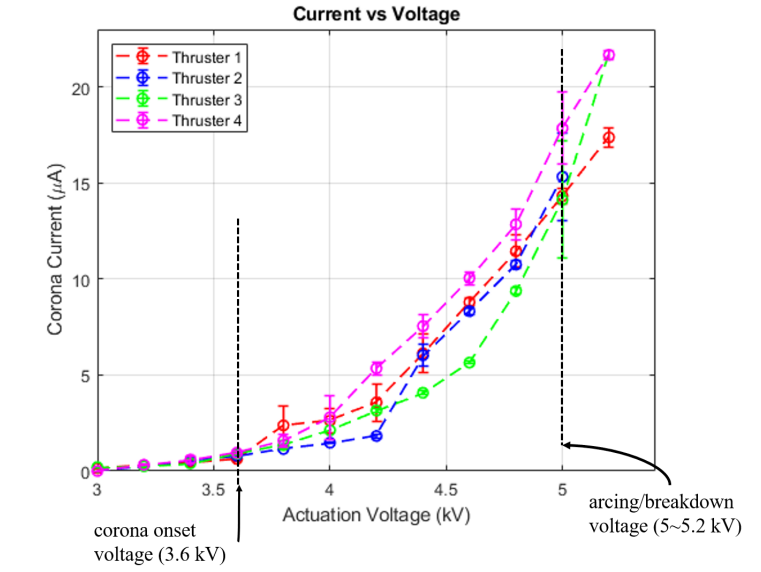

Figure 2.10: **Corona current vs the applied voltage for each individual thruster.** Measured corona onset voltage is 3600 V with a standard deviation of 100 V

Thrust measurements are made as shown in Fig. 2.11, which helped us reduce the confounding electrostatic interaction between the emitter and collector connections which was prevalent in setup depicted in Fig.2.4; A similar setup has been used in previous studies [37]. The thruster was held directly above the balance such that the collector grid was aligned parallel to the scale surface using a ceramic tweezer. This arrangement, with the thruster fixed, reduces the confounding effect of electrostatic forces acting on the aircraft through the tether wire. The distance between the collector grid and the weight scale is

21 mm. The scale reading was set to zero and each thruster was energized to measure the thrust. A piece of Teflon was placed between the balance plateau and the collector to electrically isolate the balance and to avoid any leakage current. The measured thrust is the force exerted by the accelerated ionic wind on the precision scale. It can be seen that the thrust increases with the voltage applied across the electrodes as shown in Fig. 2.12. The thrust trends follow the previously reported quadratic relationship with the applied voltage [37, 35, 43]. The maximum thrust generated occurs immediately before the sparkover is initiated, at which point thrust drops to zero and destroying the mesh. The peak force generated by each thruster was around 260 μN with a standard deviation of 20 μN.

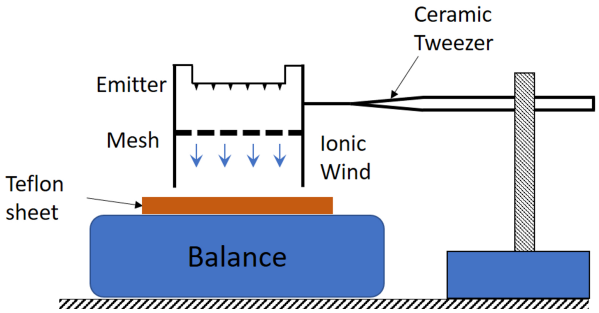

Figure 2.11: **Schematic of thrust measurement apparatus.** The thrust generated by the EHD thruster was measured by measuring the force produced by the ionic wind on the precision scale. Tethers are not shown for simplicity and the thruster is not resting on the scale.

Thrust density and efficiency are important parameters in understanding the working and performance of EHD thruster compared to other designs. Thrust density is defined as the amount of thrust generated per unit area, whereas efficiency is defined as thrust per unit power. Thrust density for EHD thrusters is calculated from the effective area where EHD flow exists, i.e., the mesh area. Fig. 2.13 shows how the thrust density varies with the corona input power of EHD thruster. The electrical power was calculated from equation 2.3.

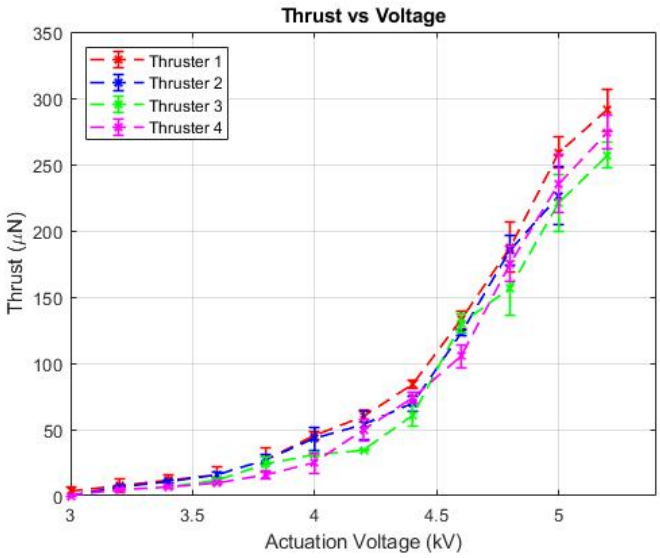

Figure 2.12: **Thrust variation with applied voltage is depicted for each thruster of the quad-thruster device.** The input voltages range from 3 kV to 5.2 kV.

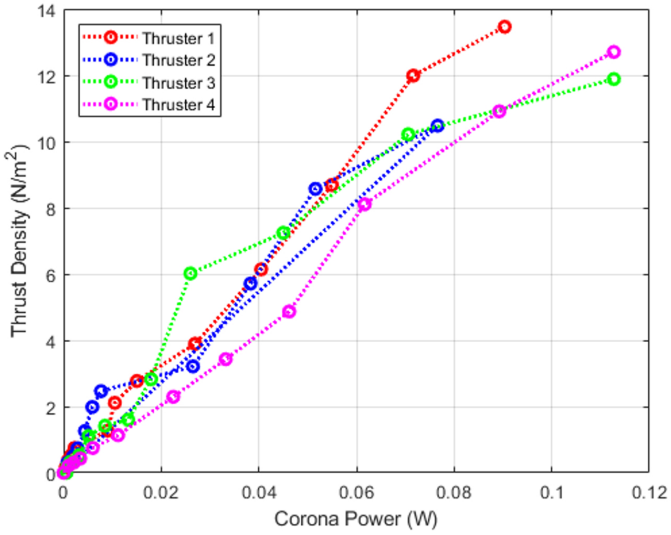

Figure 2.13: **Efficiency in terms of thrust density versus the corona power for each thruster in the quad-thruster device.** The data points shown displayed are mean values of thrust density and corona power.

For free flight experiments, the device was placed on a wooden table. The four emitters are interconnected with 51 gauge wires as mentioned above in the assembly section and the quad thruster was actuated using two 58 gauge copper wires in front of a high-speed camera (Sony RX100). One 58-gauge connection is attached from the top to one of the inner ends of an emitter and the other connection is attached to the center of the collector grid. The power tethers were held using ceramic tweezers and strain relieved. The inner legs were removed and attached to the outer legs of the thruster to increase the height and diminish the electrostatic interaction with the takeoff plane. With a voltage of 4.6 kV, lift off of quad thruster was achieved. Fig. 2.14 provides an image sequence from the flight for the first 0.32 seconds before the wires touched each other, which ended the free flight. This conclusively shows that the device can lift its weight and in the future, a vertical liftoff can be achieved by trimming the thruster as illustrated in [8].

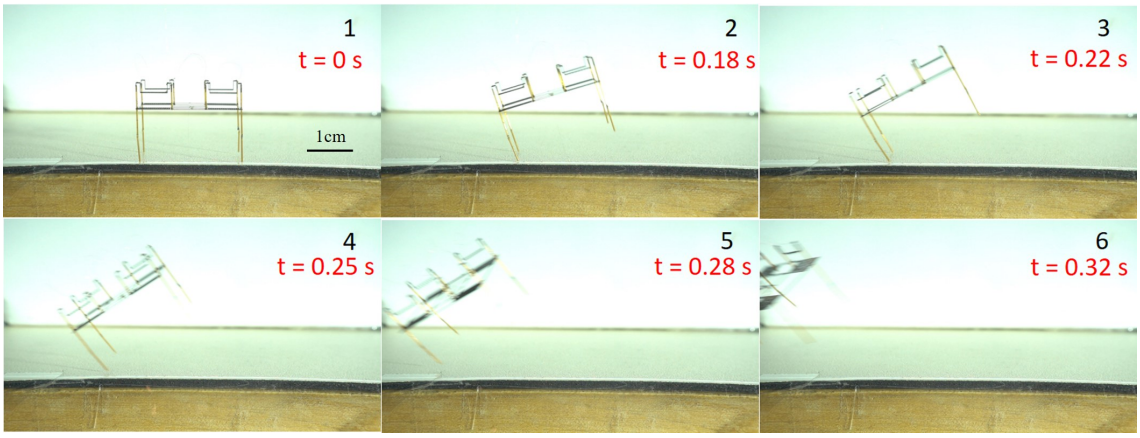

Figure 2.14: **Frames captured at a frame rate of 240 fps from the quad-thruster in flight.** The thruster is resting on the table with the collector connection dangling down and the emitter connection straight up.

2.8 Performance Comparison

2.8.1 State-of-the-art meso-scale EHD thruster-array - Ionocraft

Here, the performance of the single-emitter thrusters of our four-thruster device is compared to the single-emitter, the four-thruster device presented in [13] (which did not directly measure thrust measurements). Hence, to compare the performance of the two arrays, the thrust generated (estimated from the takeoff video presented in [13]) and thrust-to-weight ratio are chosen as the criteria. The single emitter version of the Ionocraft takes off at 2400 V with a corona current measuring close to 20 μA. This works out to a corona power of 0.048 W, and from the observed peak acceleration of the Ionocraft, they conclude that the corresponding thrust is approximately 200 μN which amounts to a thrust-to-weight ratio of 2.04. At the same input power, our quad-thruster device generates 675 μN which gives a thrust-to-weight ratio of 1.86. Table.2.1 includes a comprehensive summary of manufacturing methodology and performance comparison between the Ionocraft and our laser-fabricated quad-thruster device.

Table 2.1: **Comparison of our work with earlier work by Drew [13].**

Comparison Criterion	**Drew [13]**	**Our work**
Electrode Material	Silicon	Carbon fiber (grid) Stainless steel (emitter)
Total weight (μN)	98 μN (10 mg)	362.6 μ N (37 mg)
Thrust at 0.048 W (μN)	200 μN	675 μN
thrust-to-weight ratio at 0.048 W	2.04	1.86
Assembly time in minutes	30	15
Clean-room facility	Required	Not required

2.8.2 UW's RoboFly

Thrust density and efficiency are used to compare the performance of the EHD thruster to UW's RoboFly - a state-of-the-art flapping-wing micro-aerial-vehicle (FW-MAV). A maximum thrust of 0.295 mN corresponds to 13.67 N/m^2 thrust density achieved at an input electrical power (aka corona power) of 90.4 mW. Therefore, the thrust density per unit power for the EHD thruster is 151.17 N/m^2W. The efficiency is about 3.265 mN/W. This data can be compared to a piezo-actuated flapping-wing such as the RoboFly [7], which has a measured efficiency of 12.2 mN/W. For a thrust of 0.736 mN, an input power of 60 mW, and a 308 mm^2 effective swept area of the wing, the thrust density is 2.39 N/m^2. Therefore, the thrust density per unit power is 39.8 N/m^2W.

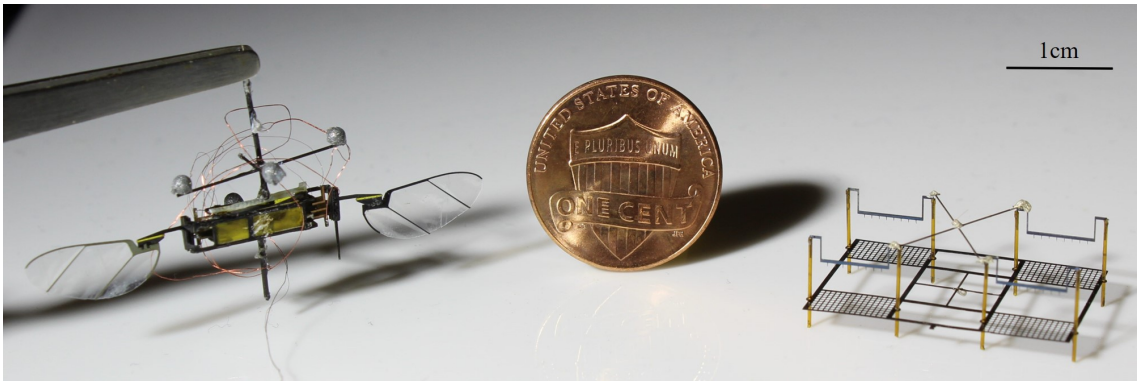

Figure 2.15: **The quad-thruster array shown next to UW's RoboFly and a US penny shown for scale.**

Therefore, while the efficiency of the EHD thruster is lower than a flapping-wing robot of comparable size (the efficiency of the flapping-wing robot is 3.74 times higher), the thrust density per unit power consumed is 3.8 times higher for the EHD thruster. This is important because the thrust density correlates to the mass of the thruster, and therefore this metric represents a scale-independent (and propulsion-type-independent) measure of efficiency.

2.8.3 To the previous Single Thruster design

The only parameter change from the previous design is the inter-electrode distance. Since we only have thrust measurements from our previous design (the high-voltage power supply used earlier didn't have an in-built ammeter), we compare the thrusting performance of a single thruster, shown in Fig.2.16. The difference in peak thrust values amount to 150.6 µN with less than 10% increase in the mass of the thruster (a mass increase of 1 mg comes from the increase in the lengths of the two glass poles and the old design has a mass of 10 mg).

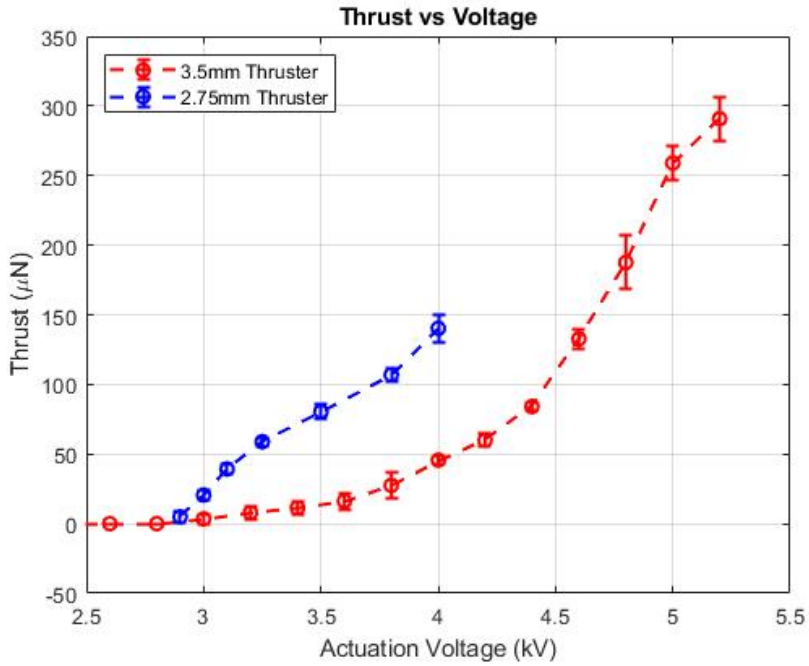

Figure 2.16: **Thrust comparison of single thrusters - d =** 2.75 mm **and** 3.5 mm

2.9 Chapter Summary

The contributions in this chapter can be summarized as follows:

- Limitations of the current design started the discussion, and systematic minor im-

provements were made to the manufacturing process of quad-thruster arrays to achieve reduced variability.

- The effects of increasing the inter-electrode distance is covered in depth. Its direct impact on thruster performance metrics such as corona current and thrust is better understood, while also validated the initial hypothesis that was put forth.

- The improvements made helped us achieve open-loop liftoff for the quad-thruster array.

- The new design was fairly compared to the state-of-the-art mesoscale robots such as UW's RoboFly (different propulsion mechanism) and Drew's Ionocraft (same propulsion mechanism). These results are published in [22].

Chapter 3

CONTROL OF MICRO-IONIC THRUSTERS

In [11], significant strides were made towards the autonomous operation of mesoscale EHD thrusters. Drew et al. used an op-amp based high-voltage amplifier to actuate their quad-thruster's collector grid with a 200 V 10 Hz peak-to-peak Sine wave signal to measure the dynamic response. The unfiltered data was Fourier transformed to show that the thruster was capable of successfully tracking inputs up to 10 Hz.
In this work, the next goal involves establishing a scheme for thrust modulation. Since the quad-thruster array is similar in control to quadcopters [33][1], high-voltage PWM is chosen as a candidate scheme to modulate the generated thrust. This chapter is organized as follows:

- High-Voltage Pulse Width Modulation
- Single Degree-of-Freedom Control Problem
- Control Results

3.1 High-Voltage Pulse Width Modulation

3.1.1 Switching Circuit

The first iteration of the high-voltage switching circuit used in this study is designed by the Sensors, Energy, and Automation Laboratory (SEAL) headed by Prof. Mamishev, is shown in Fig. 3.1.
The MOSFET IRF510 amplifies the input 5V PWM signal from the Arduino to a 13V PWM signal which is used to switch the gate of the high-voltage MOSFET IXTT02N450HV,

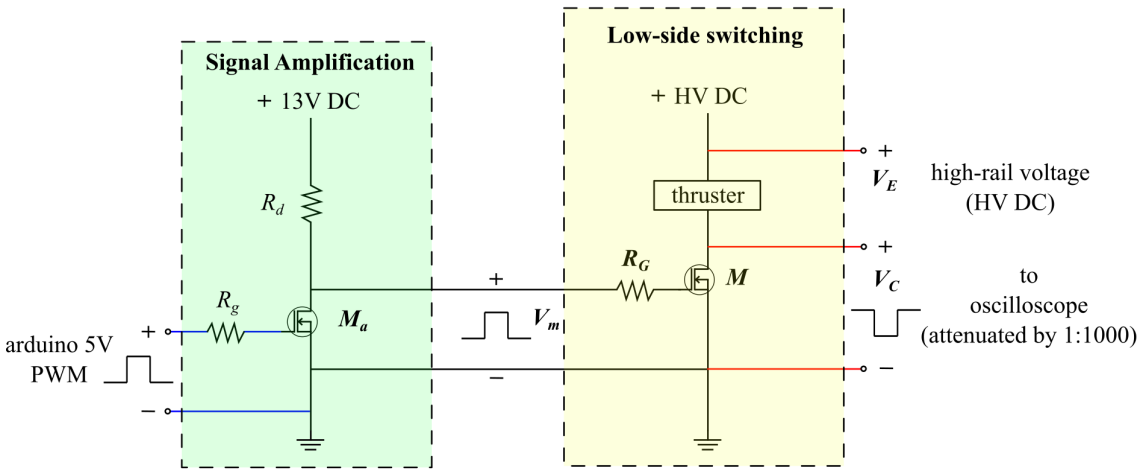

Figure 3.1: **The first iteration of the high-voltage switching circuit with two key stages are shown.** The figure shows two transistors; the first one is used for amplification and the second one is used for switching purposes.

which results in varying energizing voltage between the two electrodes. *Note: The Emitter electrode is always at the applied high-voltage in comparison to the ground. It is the Collector grid's voltage that is being switched.*

- When the input signal is high, the MOSFET is ON and the entire voltage gets applied between the Emitter and the Collector.

- When the input signal is low, the MOSFET is OFF and only a part of the voltage gets dropped across the electrodes. **The transistor can't pull-up the Collector voltage to the Emitter's level since the thruster is a very high-impedance load in comparison to the transistor's off-state.**

One serious limitation with circuit design lies in the fact that the high-voltage circuit shares a common ground with the Arduino and the computer, which retrieves data from the micro-

controller. Hence, in the following iteration an optocoupler was used to replace the voltage-amplifying transistor.

3.1.2 Circuit Changes

The modified switching circuit is shown in Fig. 3.2. It was found that a 5 V signal is more than capable of switching the high-voltage MOSFET. Hence, the optocoupler only serves the purpose of protecting the Arduino/computer side of the circuit.
Additionally, the output of the optocoupler inverts the input waveform. Hence, the off-period of the input signal determines the period of maximum thrust for a single PWM time-period.

3.1.3 Low-Voltage Test Cases

With an applied energizing voltage of 22 V, a resistive load of 2 MΩ, a 11 µA current is generated, which roughly emulates the corona current generated by a single thruster at an energizing voltage of 4.6 kV. The switching performance is shown in Fig. 3.3, where the yellow waveform is the output of the optocoupler with a high-level of 14 V. The green waveform is the energizing voltage applied at the higher end of the load and the pink waveform is the potential at the lower end of the load as a result of the transistor switching. From this switching characteristic, we can approximate the off-resistance of the transistor to around 20 MΩ
The low-voltage test case is successful, but, will not be indicative of the switching at a high-energizing voltage with the actual thruster. For example, the resistance of a single thruster with an inter-electrode distance of 3.5 mm is about 400 MΩ at an energizing voltage of 4.6 kV, which also compares poorly to our transistor off resistance of 20 MΩ. For the above conditions, we can achieve a maximum switching of 220 V. The switching transistor also has a maximum drain-source voltage rating of 4.5 kV[1]. Hence, a thruster with a

[1] `https://www.digikey.com/htmldatasheets/production/1189931/0/0/1/ixtx02n450hv.html`

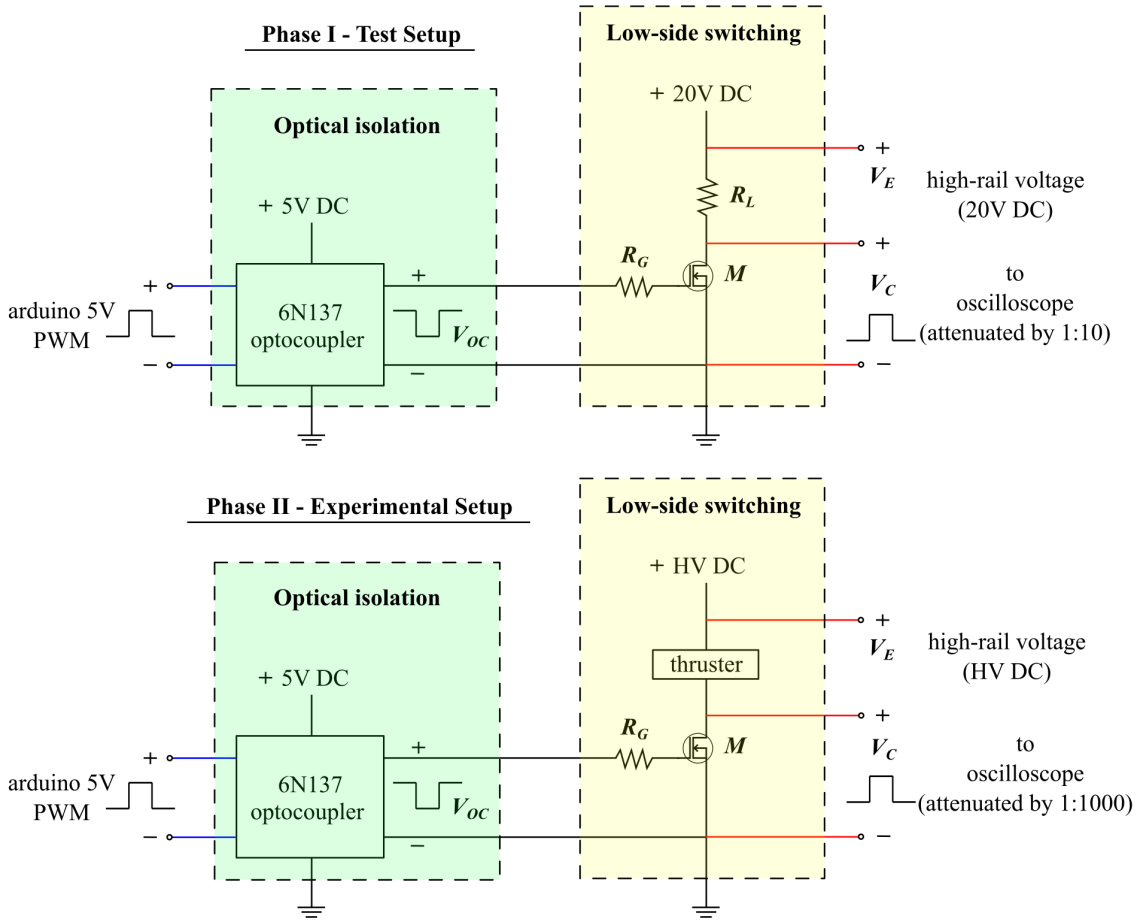

Figure 3.2: **Two testing phases of the modified switching circuit is shown.** The first testing phase is done at a low energizing voltage with a load resistance. The second phase is done at operating ranges of the thruster.

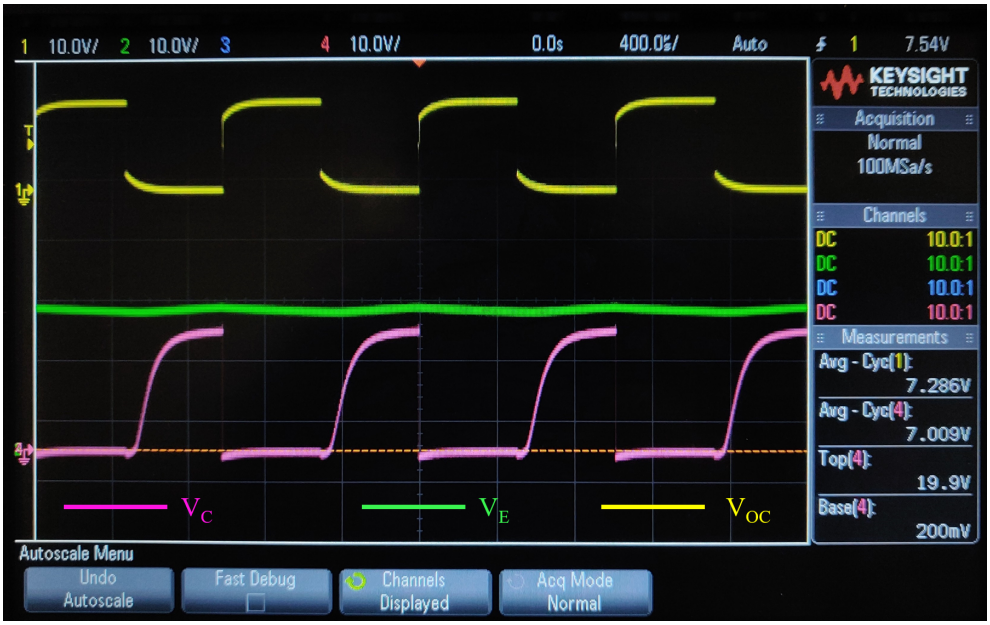

Figure 3.3: **Three waveforms show the switching performance of our low-side switching circuit for a low voltage (22 V) test case.**

higher corona current/thrust at a voltage less than 4.5 kV can help improve our switching performance.

3.1.4 Increasing the Corona Current

It has been shown that increasing the number of emitter electrodes (and hence the number of electric field localization points) significantly impacts the corona current generated [10]. This careful interplay between the space-charge density and the number of electrodes can be used to increase our current/thrust generation capabilities. In this subsection, the effect of increasing the number of emitter electrodes per thruster is explored.

The current collector gird can be divided into four regions of equal width (along 'W' as shown in Fig. 3.4) measuring 1.2 mm which has three internal equidistant nodes. These points are chosen as mounting locations for the emitter electrodes that span the length of the collector grid (depicted as 'L' in Fig. 3.4). The electrical and thrust characterization

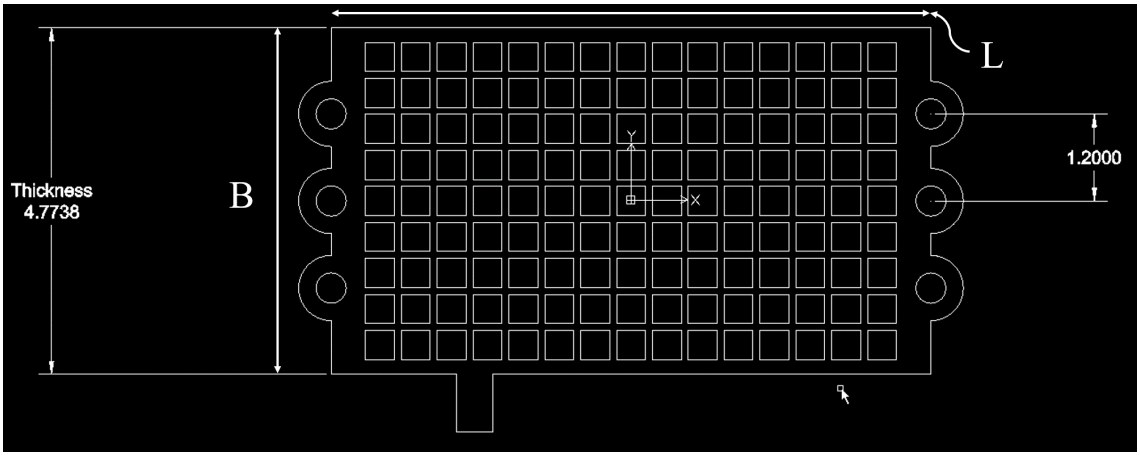

Figure 3.4: **New collector grid designed to accommodate three emitter electrodes.**

of for the new three-emitter single thruster in comparison to the normal single thruster is shown in Fig 3.5 and Fig. 3.6.

The three-electrode version of the thruster performs better than the single electrode version[2]. The current generated by the triple-emitter thruster at 4.4 kV is 1.64 times the current generated by the single-emitter version, less than the achievable current amplification and hence requires further investigation into the inter-emitter spacing.

3.1.5 Switching Characteristics

Phase two of the switching tests are conducted with the thruster and shown in Fig.3.7. The pink waveform is the voltage dropped across the MOSFET and the blue waveform is the optocoupler output. The emitter electrodes of the thruster are at 4.490 kV. For the higher duty-cycles - 50 % and 90 %, we can barely see any switching by the transistor. As we proceed to even lower duty-cycles such as 5 %, we start to see RC influenced pull-up

[2]**Note that the characterization for the three-electrode thruster was done after the control experiments were performed (which involved several trails) and have accumulated significant wear.**

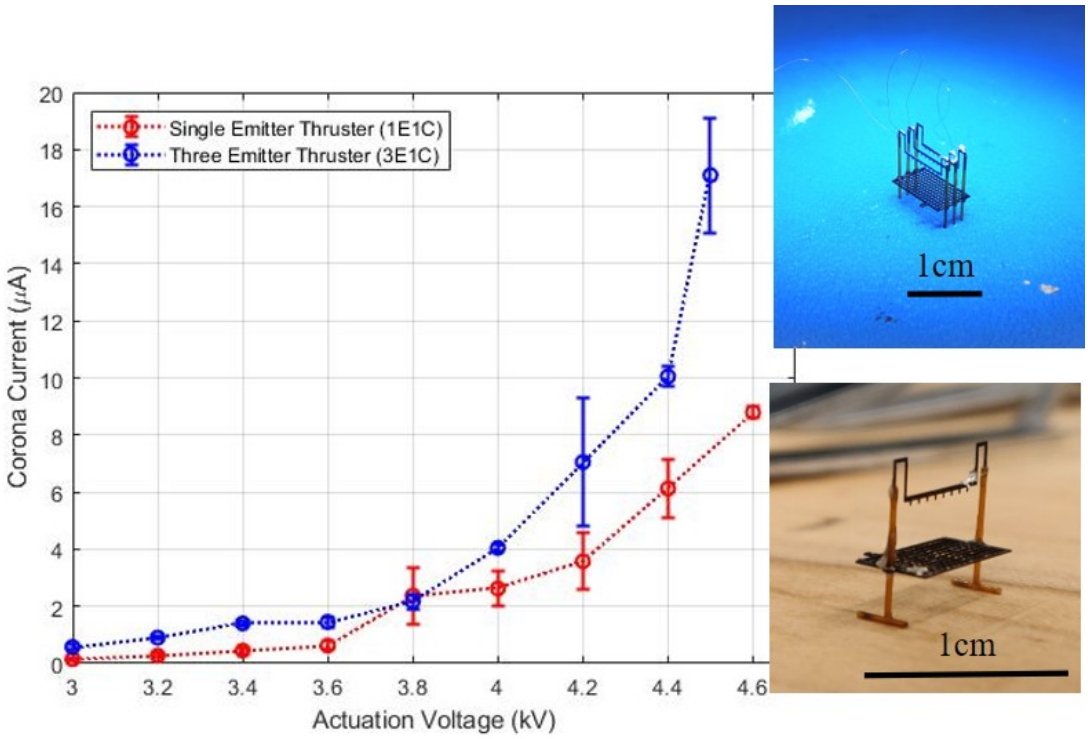

Figure 3.5: **The electrical characterization of three-emitter and single-emitter thrusters.** *Inset:* The thrusters are shown next to their corresponding plot.

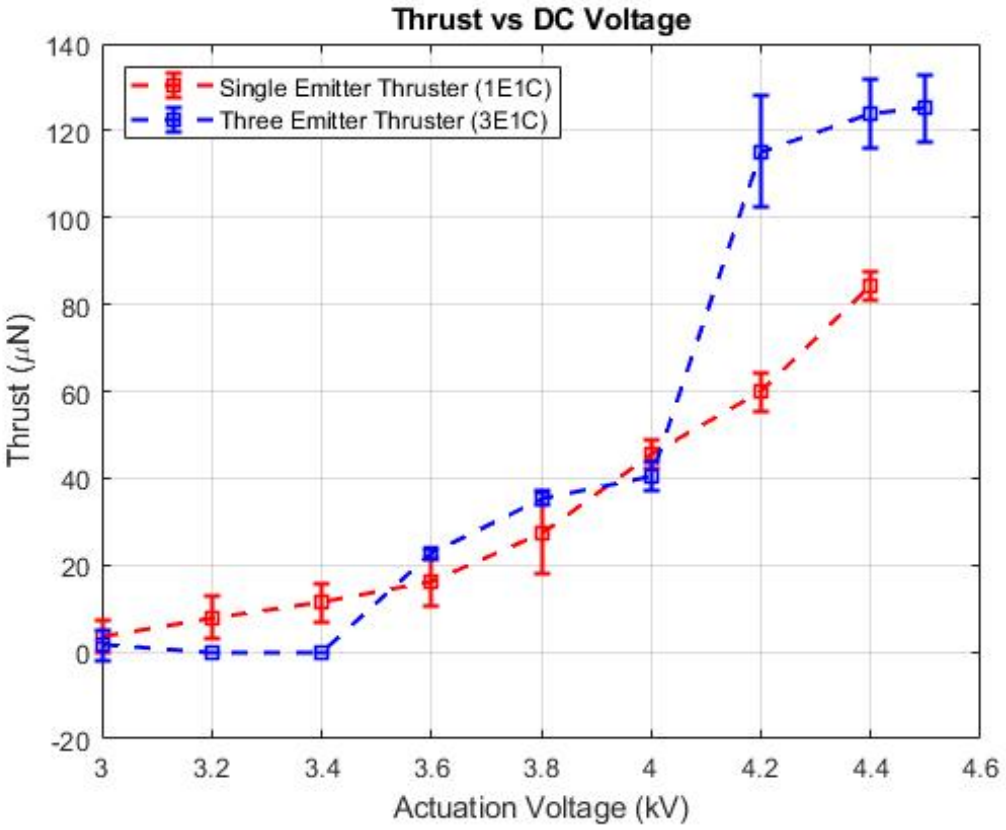

Figure 3.6: **The thrust characterization of three-emitter and single-emitter thrusters.**

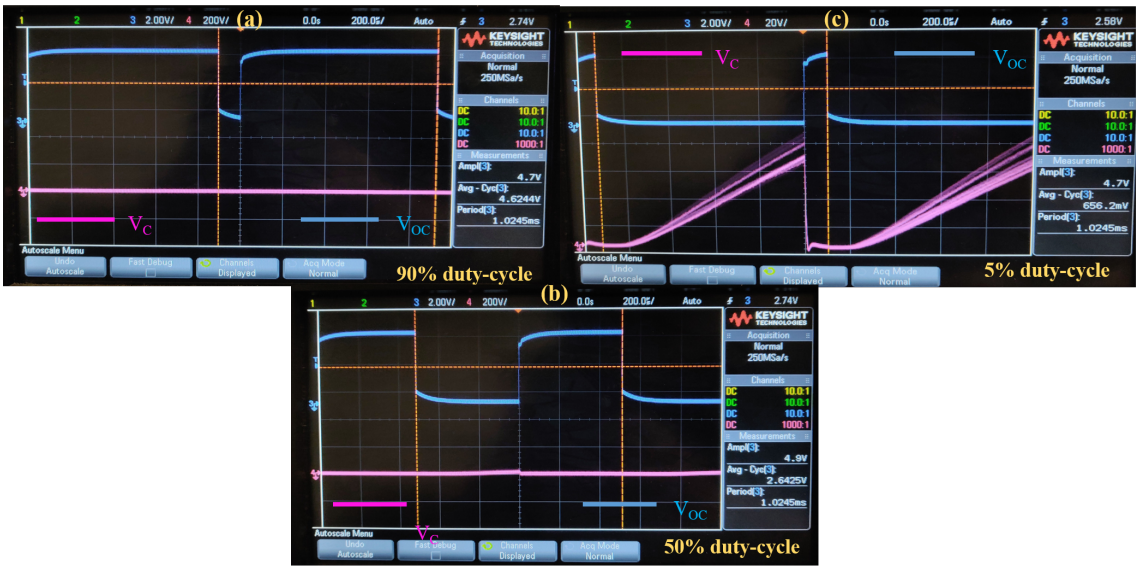

Figure 3.7: **The switching behavior is shown by the pink waveform for three different fixed duty-cycle inputs.**

when the MOSFET is switched off. The peak pull-up voltage range for various duty-cycle inputs is shown in table 3.1.

This weird behavior which we didn't see in the low-voltage test cases, can be attributed to parasitic capacitance in the circuit, primarily from the high-voltage probe which can be modeled as a resistor and capacitor in parallel. There is no real way of characterizing the switching behavior without probing this voltage drop. Also, note that the peak switching voltage varies from cycle to cycle (for the 5 % case this values varies between 65 V to 80 V). Comparing our circuit operation to dynamic voltage-divider can help shine some light on this issue (refer Fig. 3.9).

This variation in the peak pull-up voltage could be attributed to additional non-linear behavior introduced by the switching circuit or could be a result of the fluctuating thrust (fluctuating thrust/current implies fluctuating transistor resistance as shown in our voltage divider model in Fig. 3.8).

Input Duty-cycle (in %)	**Peak pull-up voltage (in V)**
0 %	200 V to 600 V
5 %	150 V
10 %	100 V
15 %	75 V to 90 V
20 %	60 V to 80 V
25 %	20 V to 40 V

Table 3.1: This table shows the peak RC-influenced pull-up voltages for different input duty-cycles.

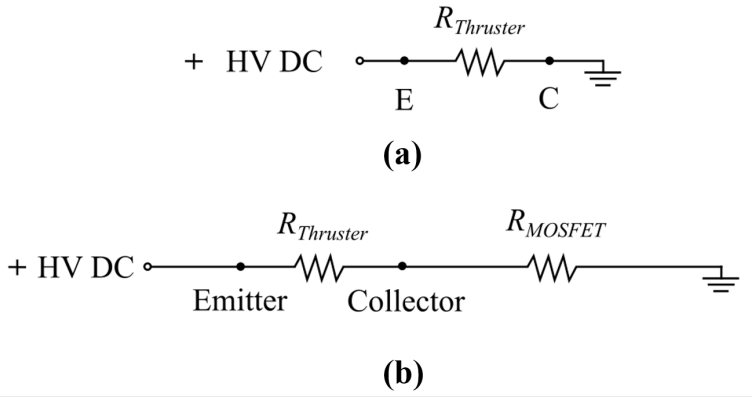

Figure 3.8: **Application of DC voltage across the electrodes is differentiated from the low-side switching case.** The drain-source resistance of the transistor switches between a high and low value.

3.1.6 Thrusting Characteristics

For characterizing our thrusting performance, we use the measuring setup illustrated in Fig. 2.4 due to its ease of execution and less time consumption. Also, data acquisition for this case was automated using an existing Simulink model which streams thrust data at a rate of 5 Hz to 10 Hz from the precision scale. For each duty-cycle value, thrust measurements for the three-emitter thruster are collected for 10.8 s. The whole range is shown in Fig. 3.9.

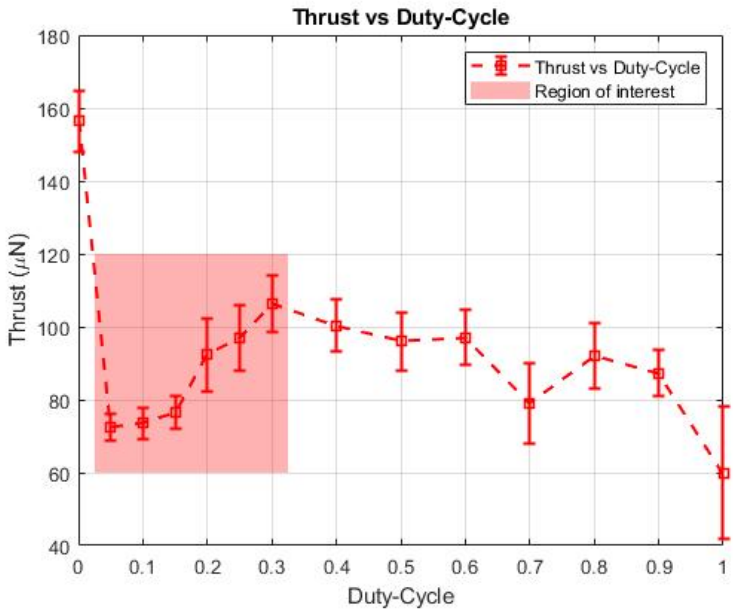

Figure 3.9: **The plot shows the variation of thrust with input duty-cycle.** The highlighted region shows favorable thrust modulation.

The thrust measurements quite strongly differ for different input values, but they do follow a linear trend for a duty-cycle range of 5 % to 30 % as shown in Fig. 3.10.

- Linear thrusting behavior will result in more effective linear feedback-controllers.
- But, the thrust also displays a large uncertainty bound due to the inherent thrust

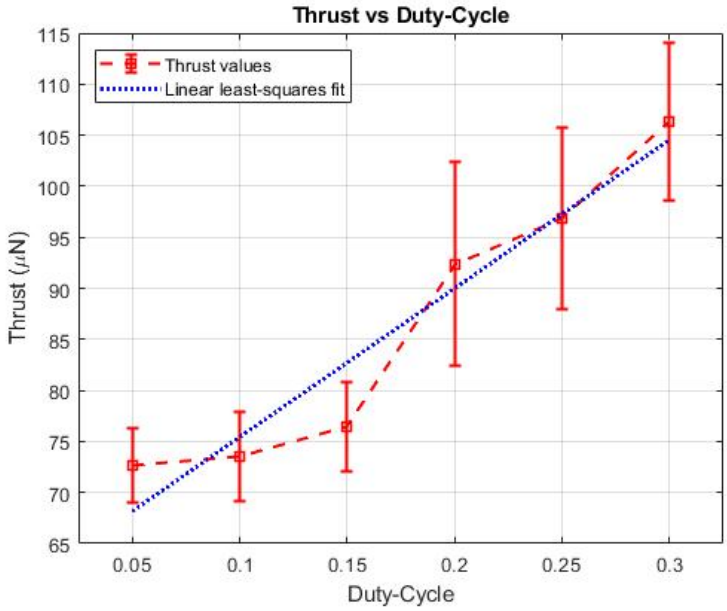

Figure 3.10: **The measured thrust exhibits a linear trend between an input duty-cycle range of** 5 % **to** 30 %**.**

fluctuations and RC influenced transistor pull-up. This will limit the performance of the feedback control system.

In this section, we have established the viability of high-voltage PWM to vary our EHD thrust. The generated thrust shows a linear trend with applied duty-cycle input but has a large uncertainty bound due to compounding non-linear effects.

3.2 Single Degree-of-Freedom Control Problem

3.2.1 Experimental Apparatus

Looking back to the development of piezoelectric actuator driven mesoscale flapping-wing MAVs, one of the first control experiments involved controlling the altitude of the robot attached to guide-wires - which was called "training wheels" for the robot [45]. In this section, the linear profile of our high-voltage PWM driven thrust modulation will be put to

the test on a simple single-degree-of-freedom control experiment. A cartoon of the apparatus is shown in Fig. 3.11 and the actual setup is shown in Fig. 3.12.

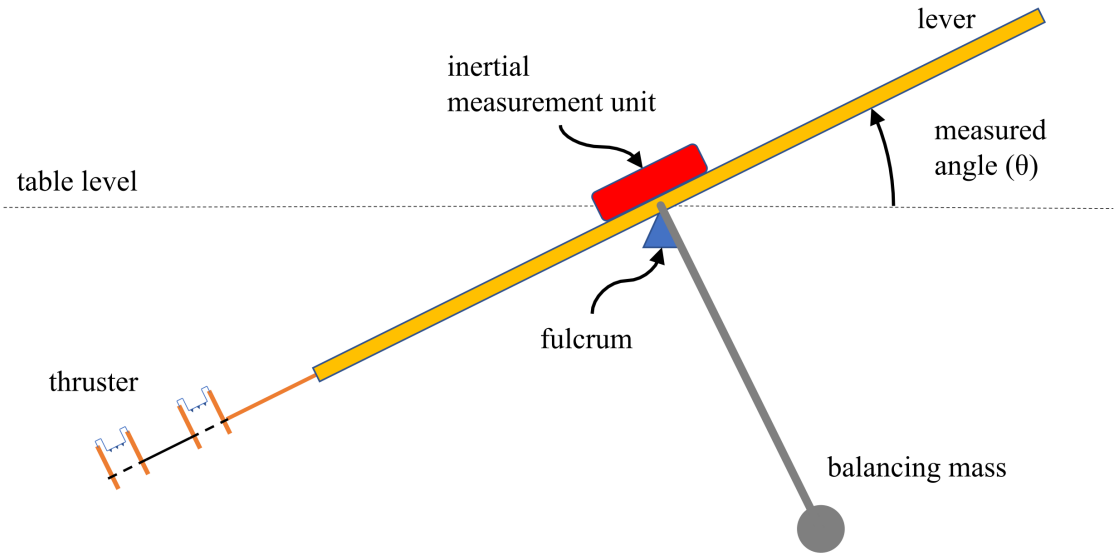

Figure 3.11: **A simple illustration showing the experimental apparatus for our 1DOF control experiment.** The IMU is mounted on top of the fulcrum and a balancing mass below it.

The basic goal of this experiment is to control the inclination angle of the lever. The IMU MPU6050 is used as our sensor to detect accelerations and angular velocities experienced by the lever. The IMU is mounted on top of the fulcrum, above the lever. This concentrates most of the mass above the rotating fulcrum and makes the system inherently unstable. Hence, to slow-down the dynamics and concentrate the overall mass at the fulcrum, we add a loop of solder as balancing mass.

One may ask why slow-down the dynamics? Firstly, the goal is to reinforce the thrust modulation results obtained in the previous section. Secondly, we aren't making any claims about the device's operational bandwidth. Such results should follow more development and optimization of the current quad-thruster design.

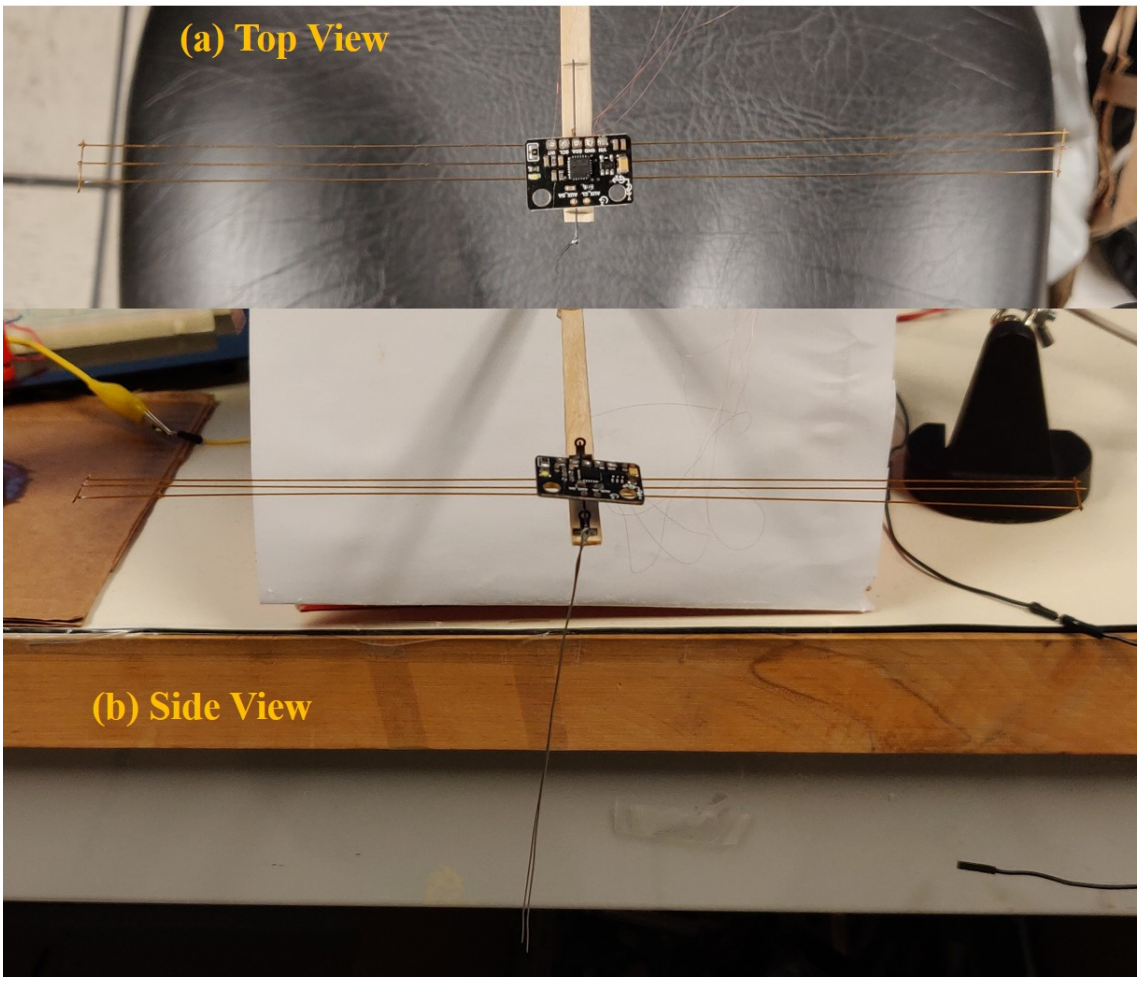

Figure 3.12: **The actual experimental setup - the lever is made up of glass capillary tubes and the fulcrum is made up of a carbon fiber rod.** The IMU MPU6050 board is mounted on top of the fulcrum rod and a loop of solder is mounted as the balancing mass below it.

3.2.2 Modeling, Controllability and Observability

We start by making a couple of simplifying assumptions.

- The IMU is assumed to be a point mass at the fulcrum.
- The balancing mass is assumed to be a point mass of mass 'm_b' at a distance of 'l_b' from the fulcrum, perpendicular to the lever.
- The thruster is assumed to be a point mass 'm_t' at a length 'l_t' along the lever and the generated thrust $1T$' is assumed to act perpendicular to the lever at all times, at this length 'l_t' (generating a clockwise moment).
- Seven electrical connections are going into and out of our system in total - five for the IMU and two for the thruster. These impose non-linear constraints on the system that aren't modeled and can be considered as disturbances or unmodeled dynamics of the system that are not important for the larger goal (especially the thruster connections strongly attract each other when powered).

It is pretty straightforward to obtain the equation of motion with θ, $\dot{\theta}$, and $\ddot{\theta}$ representing the angular acceleration, velocity, and displacement of the lever-thruster system. The moment of inertia of the system is the combination the moment of inertia of the two point-masses, $I = m_t \times {l_t}^2 + m_b \times {l_b}^2$. This is left out of the equation below for simplicity and it is made up of just time-invariant parameters (3.1).

$$I\ddot{\theta} + b\dot{\theta} + m_b g \times l_b \sin\theta - m_t g \times l_t \cos\theta = -T \times l_t \tag{3.1}$$

This non-linear dynamics is linearized as follows,

$$\ddot{\theta} = \left.\frac{\partial\ddot{\theta}}{\partial\theta}\right|_t \times \theta + \frac{\partial\ddot{\theta}}{\partial\dot{\theta}} \times \dot{\theta} + \frac{\partial\ddot{\theta}}{\partial T} \times T \tag{3.2}$$

Now, we are interested to see if this system is controllable and observable. So, let us form a two-dimensional state-space system to analyze this. Let our state vector and state-derivative vector be 'θ' and '$\dot{\theta}$' respectively. Our linear state-space system is described as follows,

$$\dot{x} = Ax + Bu,$$

$$y = Cx. \tag{3.3}$$

In the above equation, 'A' is our system matrix, 'B' is the input matrix, 'C' is the output matrix, and 'u' is the input to our system given by $u = T$ (a scalar). The matrices A and B are partials derivatives about 'θ' and 'T' respectively. C is just our sensor matrix and measures our inclination angle. After applying and simplifying (3.2), we have

$$A = \begin{bmatrix} 0 & 1 \\ (m_b l_b \cos\theta + m_t l_t \sin\theta) \times \frac{-g}{I} & \frac{-b}{I} \end{bmatrix},$$

$$B = \begin{bmatrix} 0 \\ \frac{-l_t}{I} \end{bmatrix},$$

$$C = \begin{bmatrix} 1 & 0 \end{bmatrix}. \tag{3.4}$$

The B and C matrices are time-invariant, and the A matrix is state-dependent and hence, an implicit function of time. This system gives us the following controllability '$\mathcal{C}$' and observability '$\mathcal{O}$' matrices,

$$\mathcal{C} = \begin{bmatrix} B & AB \end{bmatrix},$$

$$\implies \mathcal{C} = \frac{l_t}{I} \times \begin{bmatrix} 0 & -1 \\ -1 & \frac{b}{I} \end{bmatrix},$$

$$\mathcal{O} = \begin{bmatrix} C \\ CA \end{bmatrix},$$

$$\implies \mathcal{O} = \begin{bmatrix} 1 & 0 \\ 0 & 1 \end{bmatrix}. \tag{3.5}$$

We immediately notice that the controllability and observability matrices are state and time-independent, and have full rank. The observability matrix is an identity matrix and this means that we can observe both the states equally well (by measuring just angular displacement 'θ', we can also observe angular velocity '$\dot{\theta}$)'. Hence, we should face no issues when we are physically implementing our controller on the aforementioned apparatus. But, the physical system has some important deviations from the model to keep in mind.

- We can only thrust in one-direction (clockwise) and hence we have hard non-negative limits (typically in terms of off-duty cycle input to the switching circuit 0 % and 30 %) on the actuation that can be demanded by our control algorithm.

- Due to the previous point and apparatus build, the system is controllable only in the 110° to 250° range. This range is also further reduced by various electrical connection interaction in and out of the system (especially the high-voltage ones which strongly attract each other).

- Our sampling time will also play a key role in determining how effective our control strategy is. Are the sensor and information-processing hardware and software components fast enough to capture enough information? Is the control frequency high enough to combat the non-linear effects discussed earlier and the thrust uncertainty?

We will look at the simplest possible execution of a controller and estimator for our control problem.

3.2.3 Control System Architecture and Implementation

Due to observed linear trends in thrust generated with duty-cycle, the PID controller was chosen for its simplicity and ease of implementation. Both the estimation and control algorithm is implemented on an Arduino Mega2560 micro-controller. The schematic of the control system architecture is shown in Fig. 3.13.

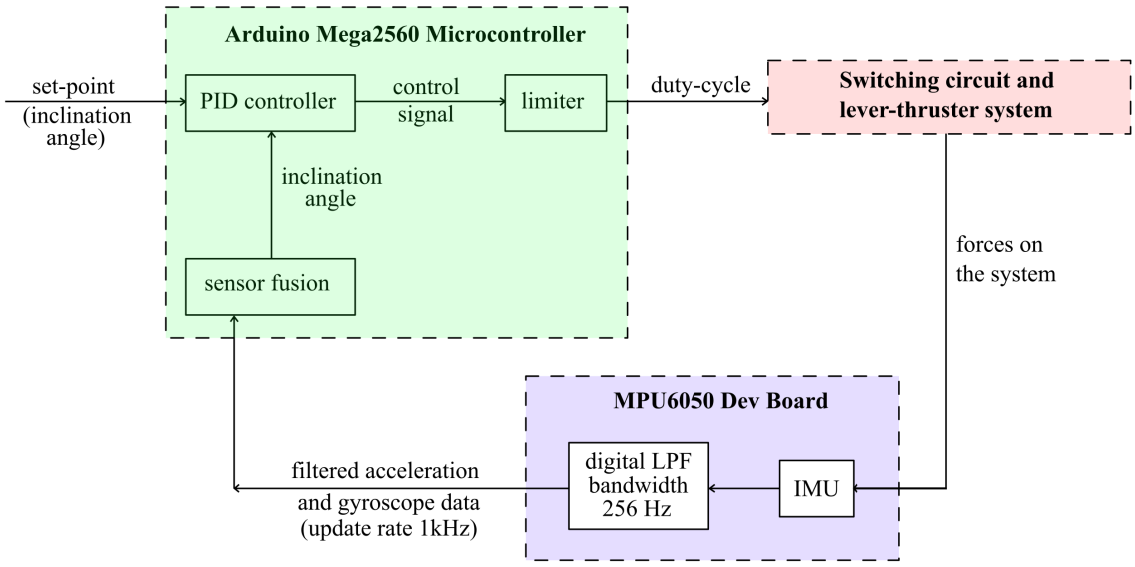

Figure 3.13: **The control system architecture for the experiment is shown.** The control and sensor-fusion estimation algorithm are run sequentially in each loop.

Acceleration and angular velocity data is recorded at 1 kHz by the IMU and is sent through an in-built digital low-pass filter with a bandwidth of 256 Hz. This filtered data is then sent to micro-controller for sensor fusion and inclination angle estimation achieved through a quaternions based approach from existing Arduino libraries for the sensor board. The outline of the micro-controller code is shown below,

```
void setup()
{
    IMU_calibrate();
```

```
}
void loop()
{
    compute_control();
    sensor_fusion();
}
```

The set-point to be tracked is set as a global variable at the beginning of the code. Since Arduino is single-threaded, we can only sequentially run our threads. Hence, in the loop, the control algorithm is run first to compute the duty-cycle input to be sent to the switching circuit. Following this, the sensor fusion algorithm is implemented sequentially to obtain the current angle, error sum, and change in angle (all global variables) from the previous loop run. Even if this control architecture is the easiest to implement, it has its disadvantages,

- Since the control algorithm and fusion algorithm are executed sequentially, this introduces some delays into our sensing thread which gets reflected in our control-action.

- To interpret and collect data from this control architecture, serial print statements are used. There will be an upper bound for the number of print statements implemented in the loop since more prints lead to FIFO overflow, more delays, loss of data packets, and in the worst-case termination of the running loop.

- This architecture bars usage more complicated control algorithms due to computational limitations and FIFO constraints as previously mentioned.

- There isn't a lot of freedom over the choice of PWM frequency and is restricted to 980 Hz and 490 Hz. This is because Arduino's analogWrite function is hard-coded to utilize the micro-controllers in-built timers. This function also only takes integer

values in range of 0 to 255 representing discretized 0 % to 30 % duty-cycle inputs respectively. Bit-banging isn't possible since we are running two different threads on a single micro-controller.

- The set-point is fixed before starting the experiment can't be changed mid-way owing to our implementation. Hence, we can only analyze the thruster performance for fixed set-point tracking.

A more involved system design would be to implement the estimation, control, and actuation in three different stages. The sensor fusion algorithm is run on one micro-controller which sends the state information to a Simulink running our control law. The computed duty-cycle input is then sent to another micro-controller to create a PWM signal through bit-banging, which gets sent to the switching circuit. Even-though having several stages could introduce latency in our control system, it has the following advantages,

- Measurements and control signals can be plotted in real-time.
- A time-varying reference can be provided to the system which could form the basis for future controlled flight experiments.
- Bit-banging for the generation of PWM signals gives us more freedom over duty-cycle and frequency.

A simple discrete-time PID control law is used to compute the input duty-cycle 'D' (limited to a range of 0 % to 25 %) sent to the switching circuit. An input value of 30 % is avoided due stray arcing events which caused loss of thrust and disrupted sensing. Desired set-point is constant for a run and is given by 'θ_d'. The angle information at the k-th time-step is given by '$\theta[k]$'. For controller gains 'K_p','K_i' and 'K_d', the discrete-time control law is as follows,

$$D = K_p \times (\theta_d - \theta[k]) + K_i \times \sum_{n=0}^{k} (\theta[k] \times h) - K_d \times \frac{(\theta_d - \theta[k])}{h} \tag{3.6}$$

Here, 'h' is the length of a time-step and in our case corresponds to the time of execution for a single loop run, which needs to be estimated in-order to work with reasonable controller gains.

3.2.4 Step Response and System Identification

As discussed in the previous section, after several trials, the number of stable serial prints that could be executed in a single loop was estimated to be two. Hence, we can transfer the current angle and current control data from the micro-controller to the MATLAB workspace. The angle data obtained from a step-response is shown in Fig. 3.14.

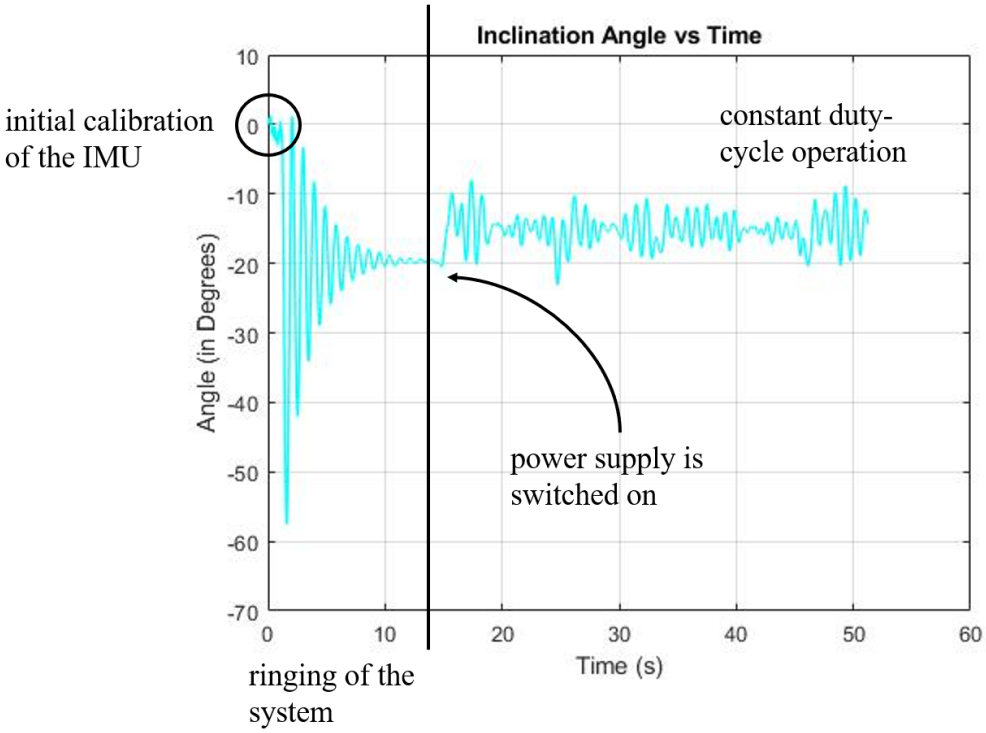

Figure 3.14: **The inclination angle data is plotted with time.** The angle data is collected in MATLAB for an input duty-cycle of 20 %

The IMU is calibrated first and then the lever is released. With the weight of the thruster attached to one end, it rings to rest at $-20°$. It is important to note that while this is happening, the controller is computing the control-action, but only a fixed duty-cycle input is sent to the switching circuit. This is needed to characterize the estimation and control frequency of the micro-controller. Now, the power supply is switched on and the input gets applied to the thruster lever system, where the system climbs to a new level and thrust fluctuations induce oscillations at many different points in time.

Since we have only two serial prints at our disposal, time-stamps are added when the data is received in MATLAB. Elapsed-time between two consecutive data packets ranges from 1 ms to 10 ms. This is averaged for a data acquisition period of 50 s, and the average sampling time turns out to be approximately 5.1 ms corresponding to a control and estimation frequency of 198 Hz. This average time-period is then used in our PID control algorithm.

From Fig. 3.15, we can immediately make the following observations,

- This canonical second-order system has a resonant frequency at 1 Hz. Stabilizing and increasing the MOI of the system through a balancing mass successfully slows down the dynamics.

- Physical systems aren't band-limited, but the spectrum above a certain point is so small that we can consider them as such. In our case, the frequency response has a magnitude of -33 dB at 20 Hz. Even if we consider this to be our bandwidth, we are still sampling approximately 10x faster (5 x to 10 x bandwidth is a rule of thumb to choose the sampling frequency) [14].

- Another thumb rule is to actuate the system at 30 x to 40 x the resonant frequency and our control frequency is much greater than this requirement.

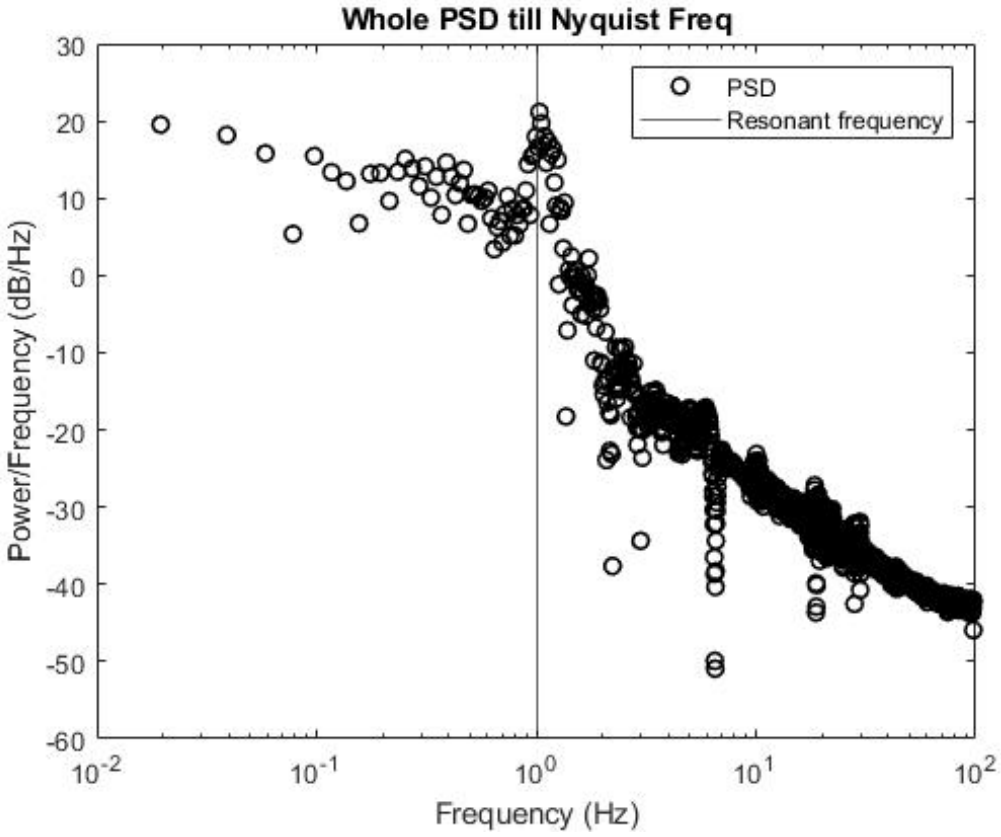

Figure 3.15: **The power spectral density of system obtained from a step-response, plotted till the Nyquist frequency.**

3.2.5 Controller On vs Off

A zoomed-in section of one of the control results is shown in Fig. 3.16 to highlight the controller on and off operation for our system.

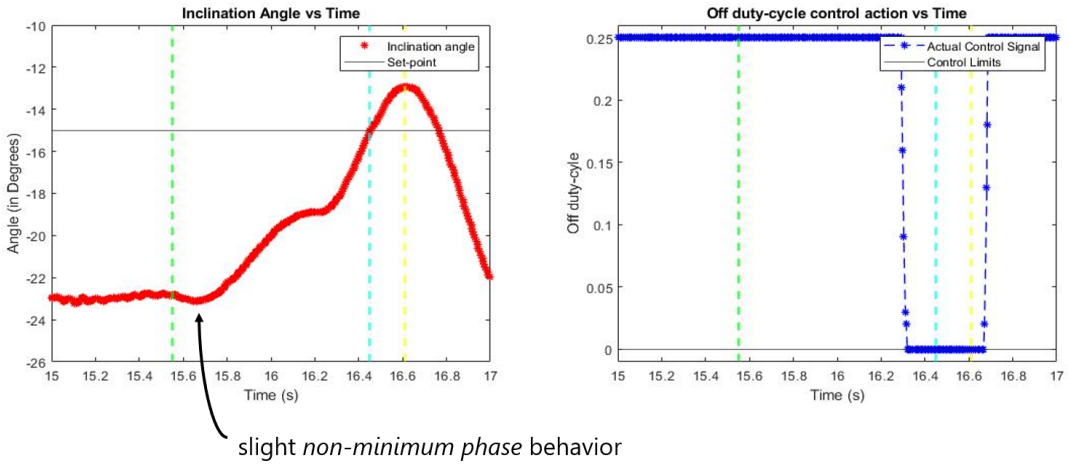

Figure 3.16: **The controller on-off case is highlighted.** The hashed-green line represents the moment the power-supply is switched on.

Once, the power supply is switched on (represented by the green hashed line in Fig. 3.16), the emitter connection gets strongly attracted to the collector connection causing an initial dip in the inclination angle which is a non-minimum phase behavior. Before, the power supply is on, we can see that the controller is commanding maximum thrust and this quickly changes as the inclination approaches and overshoots the set-point. Now we are convinced that the controller is doing what we need it to do. There is no switch for the controller since it is integrated inside the void loop and that runs without termination.

3.3 Control Results

3.3.1 High-Gain PD Control

A set-point of $-15°$ is chosen. The response for $K_p = 10, K_d = 2$ and control limits $[0.0, 0.3]$ is shown in Fig. 3.17.

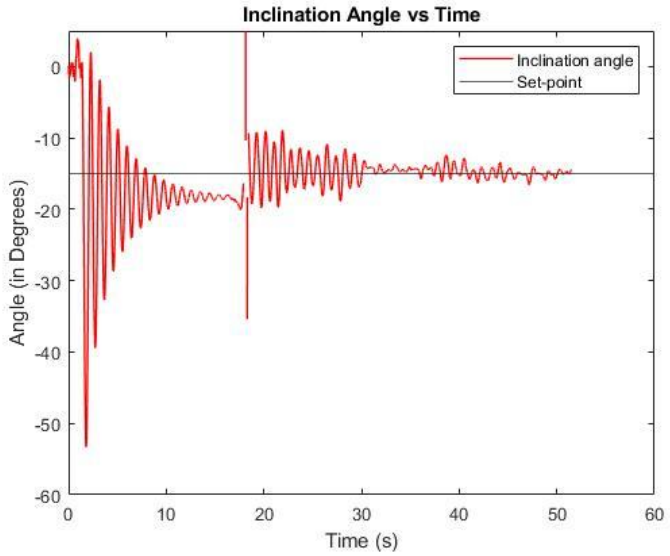

Figure 3.17: **The response for a high-gain case.** $K_p = 10, K_d = 2, \theta[0] = -19°$

The horizontal line in the plot shows the set-point to be tracked. Near the 19 s mark, we can see that the IMU data was disrupted briefly. This was caused by an arcing event between the electrodes, hinting at the fact that additional electric shielding is required. Low steady-state error is achieved after 20 s and is also the settling time for this response. With more trials, the thruster accumulates wear which leads to lower corona current and higher fluctuations. This phenomenon is not characterized in this study. After several trials, the response correlated with video for the same parameters except with an initial condition of $-23°$ is shown in Fig. 3.18.

In Fig. 3.18, we can see that after the initial ringing stops, the controller commands the maximum thrust at around 10 s to 15 s. Once the power supply is switched on, the con-

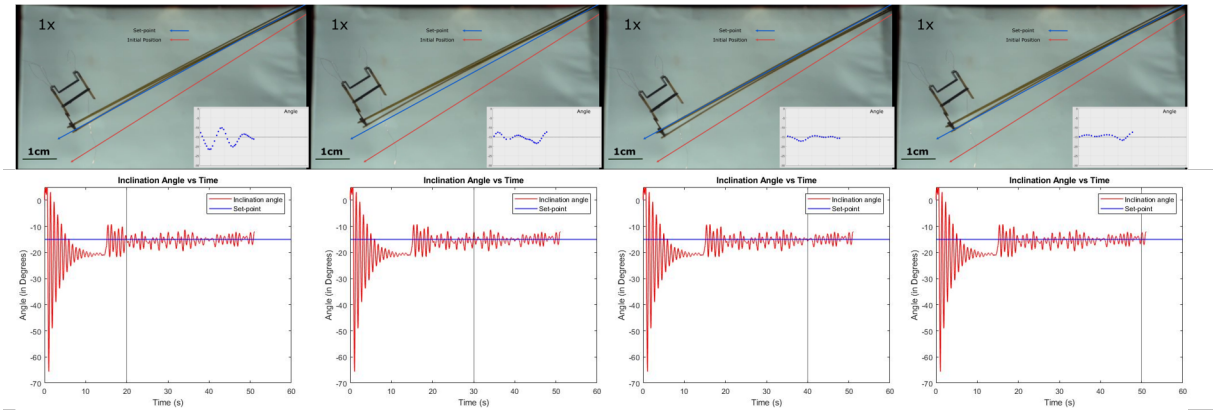

Figure 3.18: **The response for a high-gain case correlated with the video of the experiment.** $K_p = 10, K_d = 2, \theta[0] = -23°$

troller starts acting on the system. Since this is a high-gain response, the controller commands a lot of thrust at the control limits with steep climbs and drops. This comes from the interaction between the derivative controller and thrust fluctuations. *In an ideal system with zero thrust uncertainty, the PD control output should oscillate about a specific duty-cycle input and the PID control output should converge to the same input with zero steady-state error.*

A zoomed in version of the response is shown in Fig. 3.19. Here, we have three vertical lines in the response and control action plot to help us compartmentalize different sections of the response and commanded control action. Before the first line, the response is climbing and the PD controller doesn't command any action as expected - the output of the control law would be negative duty-cycle values for positive error and positive response slope which will be limited to zero (since we can only thrust is one direction). Past the first line, the response starts approaching the set-point. The derivative control action spikes regulate the downward velocity. This is clearly visible from the four spikes in control which is immediately followed by "braking" in the response.

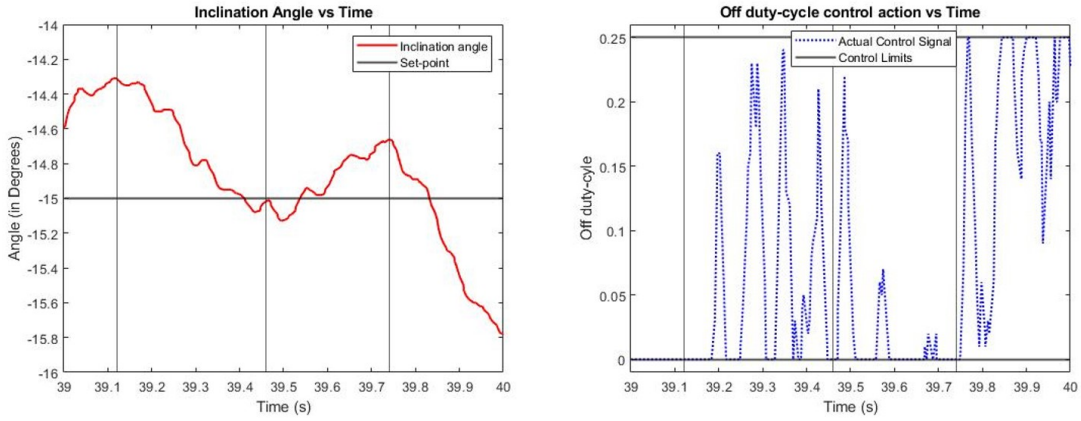

Figure 3.19: **The response for the high-gain case - zoomed into the response exhibited during a second leading up to** $t = 40\,\mathrm{s}$**.** $K_p = 10, K_d = 2, K_i = 0.05, \theta[0] = -23°$

3.3.2 Low-Gain PID Control

For the low-gain trials, the proportional and derivative gains were halved, and a small integral gain ($K_i =$) was introduced. Since we can't have an initial ringing phase where the integral control will be accruing, the balancing solder loop was bent in such a way that the lever starts from 0° position. This way, the power can be supplied as soon as the sensor is online. The angle response and control-actions are shown in Fig. 3.20.
The steady-state error and thrust fluctuations are lower than the high-gain case, but the integral control can't achieve zero steady-state error with high uncertainty in the thrust. Also, the control-action requested by the controller is more reasonable.

3.4 Chapter Summary

- A high-voltage PWM circuit was introduced, improved, and then finally its switching behavior was characterized.

- The thrust modulation achieved by this circuit was characterized for the entire duty-

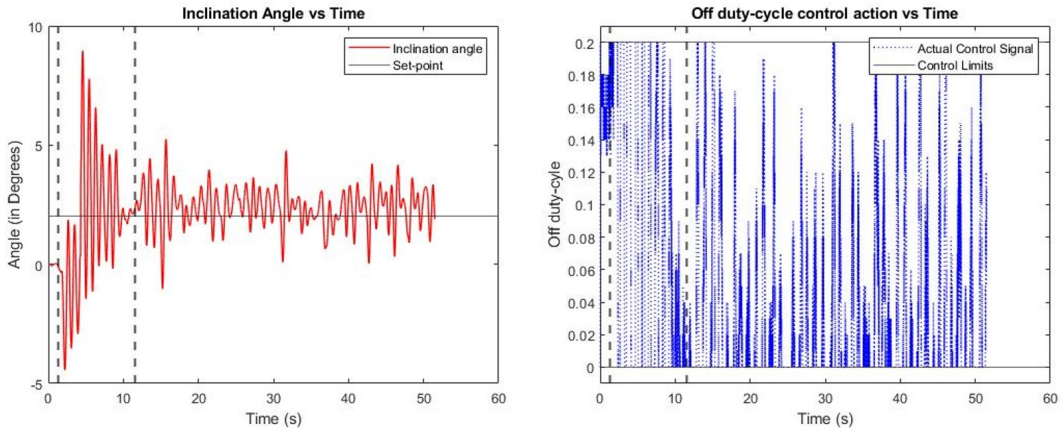

Figure 3.20: **The response and control action for a low-gain case.** $K_p = 5, K_d = 1, K_i = 0.05, \theta[0] = 0°$

cycle range and then a favorable control region was chosen based on a linear change in thrust.

- A simple 1DOF experimental apparatus was chosen to reinforce our thrust modulation results. The apparatus was explained, improvements were made to make the task more tractable by slowing down the dynamics and increasing the moment of inertia of the setup by adding a balancing mass.

- Simplest possible estimation and control architecture was considered with a 6-axis IMU - MPU6050 and Arduino Mega2560 micro-controller.

- Step-response of the system was used to obtain the average sampling time (or a single loop execution time) which is then used in the control algorithm to approximate the discrete summation of error and backward difference based change in angle. The control and estimation frequency was backed out to 198 Hz.

- The step-response data is also used to obtain the frequency response of the system. A clear resonant peak was obtained at 1 Hz. This information was used top back out

the fact that our estimation and control frequencies are well above the minimum requirement.

- The linear high-gain PD and low-gain PID controllers did a good job of tracking the reference. The high-gain PD controllers achieved much smaller steady-state error and were able to combat thrust fluctuations more effectively.

Chapter 4

FUTURE WORK

4.1 Development

Significant development has to be made before controlled flight tests are possible. In [22], we report the peak thrust-weight ratio of the quad-thruster array to be 3.03 with an operating range of 3.6 kV to 5.2 kV. The switching transistor has a maximum voltage rating of 4.5 kV, cutting down our operating range my almost half. Some changes which can help us proceed towards controlled flight experiments is discussed below.

The inter-electrode distance can be decreased to fit our new maximum dictated by the transistor. Then, we can increase the number of emitter rows, and by optimizing their spacing obtain increased thrust generation at a lower operating range.

The inter-electrode spacing is set using the spacing jig, as discussed in the second chapter. The process involves uniform physical contact of this jig with all the tips before the electrode gets glued in place. Alternate, non-contact methods of maintaining the inter-electrode spacing should be explored. One potential method could involve fixing the distance between the electrode shoulder to the collector grid, which still achieves uniform inter-electrode spacing. More precise CNC milled aluminum jigs ([11]) can substitute our CO_2 laser cut acrylic holding jig.

Full-blown constrained parametric studies and FEA analysis can be performed to analyze the EHD induced flow in the thruster. This can help us explore, the geometry of the collector grid for reduced aerodynamic drag and maximizing the density of electric field lines for higher corona current and thrust generation (due to heat-affected-zone, the DPSS laser can't make cuts with a separation less than 50 µm). Simultaneously, we can explore the effects of placing emitter tips above a grid opening or a grid line. The resulting flow struc-

ture can be compared and parameters can be optimized for increased thrust generation as shown in [13].

The cause and rate of thruster wear should be characterized. In [13], the emitter tips had tungsten coating to improve the electrode life. 100 µm thin tungsten sheets are available, and can be cut with our DPSS laser. The performance of the tungsten emitter electrode can be more favorable for future designs.

4.2 Control

The dynamic response of the thruster has to characterized to check if it has enough bandwidth for free flight. The dynamics of our experimental setup (around 1 Hz) is rather slower that the dynamics of free flight. The characterization process requires a force sensor to measure the thrust when the thruster is actuated with a pseudo-random duty-cycle input. Take the Fourier transform and computing the power spectral density can help us determine the frequency response characteristics of the thruster (similar to what was done for the experimental setup). This will also help us analyze the thrust profile with respect to the switching profile.

The switching circuit is barely able to achieve thrust modulation and at the moment not capable of completely switching off the thruster. This because of high leakage current when the transistor is switched off and hence achieves at best 200 V to 600 V of switching for the collector grid potential (in terms of the mean range of thrust - 73 µN to 106 µN). The reason for the wide noise band in our modulated thrust (refer 3.15) needs to be narrowed down - one potential cause is the switching nature of the circuit and in that a linear amplifier might be preferred instead. The PWM behavior can also be improved by adding a swamping resistor in parallel to the thruster and the collector voltage can be manually pulled up.

Finally, in order to move towards autonomous micro-ionic lifters, porting the required power-electronics onboard is a monumental challenge.

BIBLIOGRAPHY

[1] Erdinç Altuğ, James P. Ostrowski, and Camillo J. Taylor. Control of a quadrotor helicopter using dual camera visual feedback. *The International Journal of Robotics Research*, 24(5):329–341, 2005.

[2] Siuakumar Balasubramanian, Yogesh M Chukewad, Johannes M James, Geoffrey L Barrows, and Sawyer B Fuller. An insect-sized robot that uses a custom-built onboard camera and a neural network to classify and respond to visual input. In *2018 7th IEEE International Conference on Biomedical Robotics and Biomechatronics (Biorob)*, pages 1297–1302. IEEE, 2018.

[3] Yufeng Chen, Hongqiang Wang, E Farrell Helbling, Noah T Jafferis, Raphael Zufferey, Aaron Ong, Kevin Ma, Nicholas Gravish, Pakpong Chirarattananon, Mirko Kovac, et al. A biologically inspired, flapping-wing, hybrid aerial-aquatic microrobot. *Science Robotics*, 2(11):eaao5619, 2017.

[4] Bo Cheng, Xinyan Deng, and Tyson L. Hedrick. The mechanics and control of pitching manoeuvres in a freely flying hawkmoth (manduca sexta). *Journal of Experimental Biology*, 214(24):4092–4106, 2011.

[5] Kwing-So Choi, Timothy Jukes, and Richard Whalley. Turbulent boundary-layer control with plasma actuators. *Philosophical Transactions of the Royal Society A: Mathematical, Physical and Engineering Sciences*, 369(1940):1443–1458, 2011.

[6] Yogesh M Chukewad, Johannes James, Avinash Singh, and Sawyer Fuller. Robofly: An insect-sized robot with simplified fabrication that is capable of flight, ground, and water surface locomotion, 2020.

[7] Yogesh M Chukewad, Avinash T Singh, Johannes M James, and Sawyer B Fuller. A new robot fly design that is easier to fabricate and capable of flight and ground locomotion. In *2018 IEEE/RSJ International Conference on Intelligent Robots and Systems (IROS)*, pages 4875–4882. IEEE, 2018.

[8] D. Dhingra, Y. M. Chukewad, and S. B. Fuller. A device for rapid, automated trimming of insect-sized flying robots. *IEEE Robotics and Automation Letters*, 5(2):1373–1380, April 2020.

[9] D. Drew, D. S. Contreras, and K. S. J. Pister. First thrust from a microfabricated atmospheric ion engine. In *2017 IEEE 30th International Conference on Micro Electro Mechanical Systems (MEMS)*, pages 346–349, 2017.

[10] Daniel S. Drew. The ionocraft: Flying microrobots with no moving parts. 2018.

[11] Daniel S Drew, Nathan O Lambert, Craig B Schindler, and Kristofer SJ Pister. Toward controlled flight of the ionocraft: a flying microrobot using electrohydrodynamic thrust with onboard sensing and no moving parts. *IEEE Robotics and Automation Letters*, 3(4):2807–2813, 2018.

[12] Daniel S Drew and Kristofer SJ Pister. Takeoff of a flying microrobot with cots sensor payload using electrohydrodynamic thrust produced by sub-millimeter corona discharge.

[13] Daniel S Drew and Kristofer SJ Pister. First takeoff of a flying microrobot with no moving parts. In *2017 International Conference on Manipulation, Automation and Robotics at Small Scales (MARSS)*, pages 1–5. IEEE, 2017.

[14] M. Sami. Fadali and Antonio Visioli. *Digital control engineering: analysis and design*. Academic Press, 2013.

[15] S. B. Fuller, J. P. Whitney, and R. J. Wood. Rotating the heading angle of underactuated flapping-wing flyers by wriggle-steering. In *2015 IEEE/RSJ International Conference on Intelligent Robots and Systems (IROS)*, pages 1292–1299, Sep. 2015.

[16] Sawyer B Fuller. Four wings: An insect-sized aerial robot with steering ability and payload capacity for autonomy. *IEEE Robotics and Automation Letters*, 4(2):570–577, 2019.

[17] Sawyer B Fuller, Michael Karpelson, Andrea Censi, Kevin Y Ma, and Robert J Wood. Controlling free flight of a robotic fly using an onboard vision sensor inspired by insect ocelli. *Journal of The Royal Society Interface*, 11(97):20140281, 2014.

[18] Christopher K Gilmore and Steven RH Barrett. Electrohydrodynamic thrust density using positive corona-induced ionic winds for in-atmosphere propulsion. *Proceedings of the Royal Society A: Mathematical, Physical and Engineering Sciences*, 471(2175):20140912, 2015.

[19] David B Go, Raul A Maturana, Timothy S Fisher, and Suresh V Garimella. Enhancement of external forced convection by ionic wind. *International Journal of Heat and Mass Transfer*, 51(25-26):6047–6053, 2008.

[20] Yifei Guan, Ravi Sankar Vaddi, Alberto Aliseda, and Igor Novosselov. Analytical model of electro-hydrodynamic flow in corona discharge. *Physics of plasmas*, 25(8):083507, 2018.

[21] Yifei Guan, Ravi Sankar Vaddi, Alberto Aliseda, and Igor Novosselov. Experimental and numerical investigation of electrohydrodynamic flow in a point-to-ring corona discharge. *Physical Review Fluids*, 3(4):043701, 2018.

[22] Hari Krishna Hari Prasad, Ravi Sankar Vaddi, Yogesh M. Chukewad, Elma Dedic, Igor Novosselov, and Sawyer B. Fuller. A laser-microfabricated electrohydrodynamic thruster for centimeter-scale aerial robots. *Plos One*, 15(4), 2020.

[23] Elizabeth Farrell Helbling and Robert Wood. A review of propulsion, power, and control architectures ...

[24] Vikram Iyer, Rajalakshmi Nandakumar, Anran Wang, Sawyer B. Fuller, and Shyamnath Gollakota. Living iot: A flying wireless platform on live insects. In *The 25th Annual International Conference on Mobile Computing and Networking*, MobiCom '19, New York, NY, USA, 2019. Association for Computing Machinery.

[25] Noah T. Jafferis, E. Farrell Helbling, Michael Karpelson, and Robert J. Wood. Untethered flight of an insect-sized flapping-wing microscale aerial vehicle. *Nature*, 570(7762):491–495, 2019.

[26] Johannes James, Vikram Iyer, Yogesh Chukewad, Shyamnath Gollakota, and Sawyer B Fuller. Liftoff of a 190 mg laser-powered aerial vehicle: The lightest wireless robot to fly. In *2018 IEEE International Conference on Robotics and Automation (ICRA)*, pages 1–8. IEEE, 2018.

[27] NE Jewell-Larsen, CP Hsu, IA Krichtafovitch, SW Montgomery, JT Dibene, and Alexander V Mamishev. Cfd analysis of electrostatic fluid accelerators for forced convection cooling. *IEEE Transactions on Dielectrics and Electrical Insulation*, 15(6):1745–1753, 2008.

[28] Yiguang Ju and Wenting Sun. Plasma assisted combustion: Dynamics and chemistry. *Progress in Energy and Combustion Science*, 48:21–83, 2015.

[29] Vladislav Yu Khomich and Igor E Rebrov. In-atmosphere electrohydrodynamic propulsion aircraft with wireless supply onboard. *Journal of Electrostatics*, 95:1–12, 2018.

[30] Vijay Kumar and Nathan Michael. Opportunities and challenges with autonomous micro aerial vehicles. *The International Journal of Robotics Research*, 31(11):1279–1291, 2012.

[31] S. Lupashin, A. Schöllig, M. Sherback, and R. D'Andrea. A simple learning strategy for high-speed quadrocopter multi-flips. In *2010 IEEE International Conference on Robotics and Automation*, pages 1642–1648, 2010.

[32] Kevin Y Ma, Pakpong Chirarattananon, Sawyer B Fuller, and Robert J Wood. Controlled flight of a biologically inspired, insect-scale robot. *Science*, 340(6132):603–607, 2013.

[33] R. Mahony, V. Kumar, and P. Corke. Multirotor aerial vehicles: Modeling, estimation, and control of quadrotor. *IEEE Robotics Automation Magazine*, 19(3):20–32, 2012.

[34] Alexandre A Martins. Simulation of a wire-cylinder-plate positive corona discharge in nitrogen gas at atmospheric pressure. *Physics of Plasmas*, 19(6):063502, 2012.

[35] Kento Masuyama and Steven RH Barrett. On the performance of electrohydrodynamic propulsion. *Proceedings of the Royal Society A: Mathematical, Physical and Engineering Sciences*, 469(2154):20120623, 2013.

[36] Eric Moreau. Airflow control by non-thermal plasma actuators. *Journal of physics D: applied physics*, 40(3):605, 2007.

[37] Eric Moreau, Nicolas Benard, Jean-Daniel Lan-Sun-Luk, and Jean-Pierre Chabriat. Electrohydrodynamic force produced by a wire-to-cylinder dc corona discharge in air at atmospheric pressure. *Journal of Physics D: Applied Physics*, 46(47):475204, 2013.

[38] T. Moribe, H. Okada, K. Kobayashl, and M. Katayama. Combination of a wireless sensor network and drone using infrared thermometers for smart agriculture. In *2018 15th IEEE Annual Consumer Communications Networking Conference (CCNC)*, pages 1–2, 2018.

[39] J Reece Roth. Aerodynamic flow acceleration using paraelectric and peristaltic electrohydrodynamic effects of a one atmosphere uniform glow discharge plasma. *Physics of plasmas*, 10(5):2117–2126, 2003.

[40] Otmar M Stuetzer. Ion drag pressure generation. *Journal of Applied physics*, 30(7):984–994, 1959.

[41] John S Townsend. Xi. the potentials required to maintain currents between coaxial cylinders. *The London, Edinburgh, and Dublin Philosophical Magazine and Journal of Science*, 28(163):83–90, 1914.

[42] John Sealy Townsend. *Electricity in gases*. 1915.

[43] Ravi Sankar Vaddi, Yifei Guan, Alexander Mamishev, and Igor Novosselov. Analytical model for electrohydrodynamic thrust. *arXiv preprint arXiv:2002.11662*, 2020.

[44] Ravi Sankar Vaddi, Yifei Guan, and Igor Novosselov. Particle dynamics in corona induced electro-hydrodynamic flow. *arXiv preprint arXiv:1902.02986*, 2019.

[45] R. J. Wood. The first takeoff of a biologically inspired at-scale robotic insect. *IEEE Transactions on Robotics*, 24(2):341–347, 2008.

[46] Robert J Wood, Ben Finio, Michael Karpelson, Kevin Ma, Néstor Osvaldo Pérez-Arancibia, Pratheev S Sreetharan, Hiro Tanaka, and John Peter Whitney. Progress on 'pico'air vehicles. *The International Journal of Robotics Research*, 31(11):1292–1302, 2012.

[47] Haofeng Xu, Yiou He, Kieran L Strobel, Christopher K Gilmore, Sean P Kelley, Cooper C Hennick, Thomas Sebastian, Mark R Woolston, David J Perreault, and Steven RH Barrett. Flight of an aeroplane with solid-state propulsion. *Nature*, 563(7732):532, 2018.

[48] K Yanallah and F Pontiga. A semi-analytical stationary model of a point-to-plane corona discharge. *Plasma Sources Science and Technology*, 21(4):045007, 2012.

[49] Yu Zhang, Lijuan Liu, Yang Chen, and Jiting Ouyang. Characteristics of ionic wind in needle-to-ring corona discharge. *Journal of Electrostatics*, 74:15–20, 2015.

Appendix A

APPENDIX

A.1 Arduino Code - Estimation and Control

```
// NEEDED FOR DUE AND MEGA - Hari
#ifndef _BV
#define _BV(n) (1<<(n))
#endif

/* CONSTANT DUTY CYCLE OPERATION - BIT BANGING
const float f = 1000; // %%%%%%%%%% PWM Frequency %%%%%%%%%%
const float D_off = 0.2;  // %%%%%%%%%% Duty Cycle %%%%%%%%%%

// Uign T_off based computation because of the O/C inversion.
// Computing time period and delay period
const float T    = (1/f)*1000*1000;       // Time period in microseconds.
const float T_OFF    = D_off*T;           // Time OFF in microseconds.
const float T_ON   = T - T_OFF;           // Time ON in microseconds.
*/


// Data logging in Matlab gives me a sampling frequency of about ~198Hz with
// an assoicated time period of 5.1ms : 0.0051s
const float T = 0.0051;
// Variables for closed-loop PID control:
```

```
//gains
float Kp = 5; // Proportional
float Kd = 1; // Derivative
float Ki = 0.05; // Integral - tune this real-time and at the very end.
//instantaneous error, acuumulating error, error_deriv initialization
//and previous angle:
float error_sum = 0;  // Initialize discretely summed error
float angle_diff = 0;   // Intialize diff in angle
//(diff in error not needed)
float error_curr = 0;   // Initialize current angle
float prev_ang   = 0;   // Initialize previous angle

//setpoint for control
float S = 2*(M_PI/180);          // ENTER IN DEGREES

//pwm output pin
int pwm_pin = 4;         // PWM pin using analogWrite().
//Duty cycle variables
float D_off = 1.00;
float D_on = 1 - D_off;

#include "I2Cdev.h"

#include "MPU6050_6Axis_MotionApps20.h"
//#include "MPU6050.h" // not necessary if using MotionApps include file

#if I2CDEV_IMPLEMENTATION == I2CDEV_ARDUINO_WIRE
```

```
    #include "Wire.h"
#endif

MPU6050 mpu;
//MPU6050 mpu(0x69); // <-- use for AD0 high

#define OUTPUT_READABLE_EULER


#define INTERRUPT_PIN 2  // use pin 2 on Arduino Uno & most boards
#define LED_PIN 13 // (Arduino is 13, Teensy is 11, Teensy++ is 6)
bool blinkState = false;

// MPU control/status vars
bool dmpReady = false;  // set true if DMP init was successful
uint8_t mpuIntStatus;   // holds actual interrupt status byte from MPU
uint8_t devStatus;      // return status after each device operation
                        //(0 = success, !0 = error)
uint16_t packetSize;    // expected DMP packet size (default is 42 bytes)
uint16_t fifoCount;     // count of all bytes currently in FIFO
uint8_t fifoBuffer[64]; // FIFO storage buffer

// orientation/motion vars
Quaternion q;           // [w, x, y, z]
quaternion container
float euler[3];         // [psi, theta, phi]
Euler angle container
```

```
// ================================================================
// ===                      INTERRUPT DETECTION ROUTINE
===
// ================================================================

volatile bool mpuInterrupt = false;
void dmpDataReady() {
    mpuInterrupt = true;
}



// ================================================================
// ===                            INITIAL SETUP
===
// ================================================================

void setup() {
    //Serial.begin(250000);
    pinMode(pwm_pin, OUTPUT); //- Duty-cycle setup.
    // COMMENT IMU SETUP
    // join I2C bus (I2Cdev library doesn't do this automatically)
    #if I2CDEV_IMPLEMENTATION == I2CDEV_ARDUINO_WIRE
        Wire.begin();
        Wire.setClock(300000); // 300kHz I2C clock.
```

```
    // Disabled on Due.
//#elif I2CDEV_IMPLEMENTATION == I2CDEV_BUILTIN_FASTWIRE
    //Fastwire::setup(400, true);
#endif
Serial.begin(250000); //115200
while (!Serial);

// initialize device
//Serial.println(F("Initializing I2C devices..."));
mpu.setSleepEnabled(false);
mpu.initialize();
pinMode(INTERRUPT_PIN, INPUT);

// load and configure the DMP
//Serial.println(F("Initializing DMP..."));
devStatus = mpu.dmpInitialize();

// supply your own gyro offsets here, scaled for min sensitivity
mpu.setXGyroOffset(121);
mpu.setYGyroOffset(-6);
mpu.setZGyroOffset(-53);
mpu.setZAccelOffset(1774); // 1688 factory default for my test chip
mpu.setXAccelOffset(1206); //  The last two added by Hari.
mpu.setYAccelOffset(-543);

// make sure it worked (returns 0 if so)
if (devStatus == 0) {
```

```
        // Calibration Time: generate offsets and calibrate our MPU6050
        mpu.CalibrateAccel(6);
        mpu.CalibrateGyro(6);
        mpu.setDMPEnabled(true);
        attachInterrupt(digitalPinToInterrupt(INTERRUPT_PIN),
        dmpDataReady, RISING);
        mpuIntStatus = mpu.getIntStatus();

        // set our DMP Ready flag so the main loop() function knows it's okay
        //Serial.println(F("DMP ready! Waiting for first interrupt..."));
        dmpReady = true;

        // get expected DMP packet size for later comparison
        packetSize = mpu.dmpGetFIFOPacketSize();
    } else {
        // ERROR!
        // 1 = initial memory load failed
        // 2 = DMP configuration updates failed
        // (if it's going to break, usually the code will be 1)
        //Serial.print(F("DMP Initialization failed (code "));
        //Serial.print(devStatus);
        //Serial.println(F(")"));
    }
}
```

```
// ================================================================
// ===                      MAIN PROGRAM LOOP
===
// ================================================================

void loop()
{
    /* FIXED D_CYCLE TESTING:
    D_off = 0.25;
    D_on  = 1-D_off;
    analogWrite(pwm_pin, int(D_on*255));
    */

    // . PD location 1. - Not using integral control.
    // Using integral control now.
    // Compute the off-precentage using the error info.
    // COMMENT PID CONTROLLER.
    D_off = Kp*error_curr - Kd*angle_diff + Ki*error_sum;
    if (D_off > 0.20)
      {
        D_off = 0.20;
      }
    else if (D_off < 0.0)
      {
        D_off = 0.0;
      }
    D_on = 1 - D_off; // Compute the ON percentage.
```

```
  // Setup the PWM using analogWrite()
  analogWrite(pwm_pin, int(D_on*255));
  //if (!dmpReady) return;

  while (!mpuInterrupt && fifoCount < packetSize) {
      if (mpuInterrupt && fifoCount < packetSize) {
        // try to get out of the infinite loop
        fifoCount = mpu.getFIFOCount();
      }

  }

  // reset interrupt flag and get INT_STATUS byte
  mpuInterrupt = false;
  mpuIntStatus = mpu.getIntStatus();

  // get current FIFO count
  fifoCount = mpu.getFIFOCount();
  //
if(fifoCount < packetSize){
while (fifoCount < packetSize) fifoCount = mpu.getFIFOCount();
}
  else if ((mpuIntStatus & _BV(MPU6050_INTERRUPT_FIFO_OFLOW_BIT))
  || fifoCount >= 1024) {
      // reset so we can continue cleanly
      mpu.resetFIFO();
  } else if (mpuIntStatus & _BV(MPU6050_INTERRUPT_DMP_INT_BIT)) {
```

```
        // read a packet from FIFO
while(fifoCount >= packetSize){
  mpu.getFIFOBytes(fifoBuffer, packetSize);
  fifoCount -= packetSize;
}

        #ifdef OUTPUT_READABLE_EULER
            mpu.dmpGetQuaternion(&q, fifoBuffer);
            mpu.dmpGetEuler(euler, &q);
            Serial.println("");
            Serial.print(euler[1]* 180/M_PI); //in rad now (* 180/M_PI).
            Serial.print(" ");
            Serial.print(S* 180/M_PI); //in rad. *180/M_PI

            /**/
            /*
            Serial.print(" ");
            Serial.print(error_curr);
            /* Not using Integral Control.
            Serial.print(" ");
            Serial.print(error_sum);
            */
            /*
            Serial.print(" ");
            Serial.print(angle_diff);
            */
```

```
            /*
            Serial.print(" ");
            Serial.print(D_off); // error change
            */
        #endif
    }
    //setupC - check inst error, error_sum and ang_deriv.
    // Compute angle change first and then
    //update the current error (e@t-1 + e_d)
    angle_diff = (euler[1] - prev_ang)/T; // T seconds
    error_curr = S - euler[1];
    error_sum += error_curr*T;
    prev_ang   = euler[1];
}
```

A.2 Data Access

Anyone with the following link can access the data associated with this research: `https://drive.google.com/drive/folders/1s20icakbE9zMjn31sdCTphu1yIhiZ4Uk?usp=sharing` It also has the MATLAB code which will recreate all the plots presented in this thesis.

NOTE: Please just download the data to play around with the matlab code which is also a part of this shared folder. And for the thrust PWM-characteristics data, the mass is negative since reduction in mass of the holding apparatus is measured (refer Fig. 2.4).